

RESEARCH ARTICLE SUMMARY

INNATE IMMUNITY

Cellular RNA interacts with MAVS to promote antiviral signaling

Nandan S. Gokhale*, Russell K. Sam, Kim Somfleth, Matthew G. Thompson, Daphnée M. Marciñiak, Julian R. Smith, Emmanuelle Genoyer, Julie Eggenberger, Lan H. Chu, Moonhee Park, Steve Dvorkin, Andrew Oberst, Stacy M. Horner, Shao-En Ong, Michael Gale Jr., Ram Savan*

INTRODUCTION: Innate immunity is crucial for defense against RNA viruses and involves sentinel proteins, such as those in the RIG-I-like receptor (RLR) family. These proteins sense viral RNA motifs, leading to the activation of type I and III interferons (IFNs), which establish an antiviral state and prime adaptive immunity. Although a strong innate antiviral response is essential for controlling infections, its dysregulation can cause tissue damage and contribute to autoimmune diseases. Thus, antiviral immune signaling needs to be balanced for effective immune defense without tissue pathology. Upon detecting viral RNA in the cytosol, the RLRs RIG-I and MDA5 translocate to contact sites between the endoplasmic reticulum and mitochondria, triggering the oligomerization of the adaptor protein, mitochondrial antiviral signaling protein (MAVS). MAVS serves as a platform for multiple signaling proteins, forming the MAVS signalosome, which leads to the activation of the transcription factors interferon regulatory factor 3 (IRF3) and nuclear factor κ B (NF- κ B) to induce IFNs and antiviral gene programs.

RATIONALE: Although protein-protein interactions and posttranslational modifications are critical for antiviral signaling through the

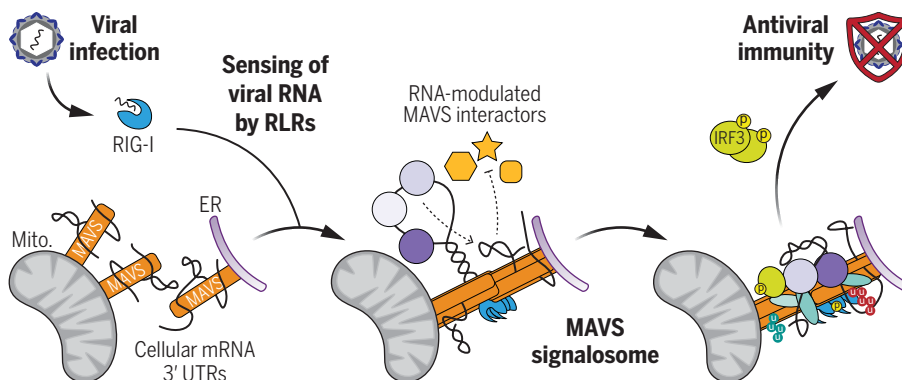
MAVS signalosome, the role of cellular RNA molecules in this process is unknown. Research over the past decade has revealed that a large and growing proportion of proteins and protein complexes can interact with RNA, often through disordered or uncharacterized domains. Therefore, the function of most RNA-protein interactions in cells remains unexplored. RNA interaction can modify protein complex function allosterically or by acting as guides, chaperones, or scaffolds, but how RNA influences the formation and function of immune signaling platforms has not been revealed. With this study, we aimed to explore how cellular RNA binding impacts antiviral signaling through MAVS.

RESULTS: We found that phosphorylation of the transcription factor IRF3 following activation of the MAVS signalosome in response to RLR signaling was decreased by ribonuclease (RNase) treatment. Likewise, phosphorylation of the transcription factor NF- κ B p65 in response to MAVS activation was also lower in the presence of RNase. This suggested that cellular RNA could contribute to the activation of the MAVS signalosome. By using sucrose gradient ultracentrifugation, we found that the density of the activated MAVS signalosome, ac-

tivated either through RLR-dependent detection of viral RNA or by MAVS overexpression in the absence of viral RNA, differed in the absence and presence of RNase treatment, suggesting that MAVS bound to cellular RNA directly. Both human and murine MAVS interacted with RNA. The MAVS-RNA interaction, as well as its function in IRF3 phosphorylation, was independent of the RLRs RIG-I and MDA5 and was intact in cells that were deficient in RIG-I and MDA5. By using infrared dye crosslinking and immunoprecipitation (irCLIP) to investigate a series of MAVS protein mutants, we showed that MAVS directly interacted with RNA through a large central domain with conserved disorder. This intrinsically disordered region was both necessary and sufficient for MAVS-RNA association, and neither the N-terminal caspase activation and recruitment domain nor the C-terminal transmembrane domain that dictates subcellular localization were required for RNA binding. From APOBEC1-mediated profiling, we found that MAVS preferentially interacted with the 3' untranslated regions (UTRs) of more than 100 cellular mRNAs, including those of the IFN-stimulated transcripts *IFIT2* and *PMAIPI*.

We used mass spectrometry to identify the proteins that interacted with MAVS in the absence or presence of RNase treatment. We identified proteins that had increased and decreased interactions with MAVS in the presence of RNA and performed small interfering RNA screens to investigate whether they altered IFN induction after RLR activation. Expression of GPX8, GDI2, RAB13, ZNF622, all of which promoted IFN induction, were required to restrict replication of vesicular stomatitis virus in cells.

CONCLUSIONS: This study uncovered a role for cellular RNA in promoting MAVS signalosome function and, consequently, antiviral signaling initiated by RLRs. Although MAVS lacks a canonical RNA-binding domain, our data suggest that its disordered domain allows it to interact with RNA, thereby potentiating RNA-modulated associations with factors required for a maximal antiviral response. Our work adds an important regulatory layer to MAVS signaling and highlights the possibility of similar RNA-centric regulation of other immune signaling complexes. With RNA increasingly seen as both a drug and druggable target, this opens the potential for RNA-based therapeutics for combating both infection and autoimmunity. ■



RNA regulatory control of the MAVS signalosome. The adaptor protein MAVS binds to the 3'UTRs of cellular mRNAs through its central disordered region. After sensing of viral RNA by RLRs, cellular RNA promotes antiviral signaling through the MAVS signalosome by altering MAVS association with RNA-modulated MAVS-interacting factors. Mito., mitochondria; ER, endoplasmic reticulum.

The list of author affiliations is available in the full article online.

*Corresponding author. Email: ngokhale@uw.edu (N.S.G.); savanram@uw.edu (R.S.).

Cite this article as N. S. Gokhale et al., *Science* **386**, eadl0429 (2024). DOI: 10.1126/science.adl0429

S READ THE FULL ARTICLE AT
<https://doi.org/10.1126/science.adl0429>

RESEARCH ARTICLE

INNATE IMMUNITY

Cellular RNA interacts with MAVS to promote antiviral signaling

Nandan S. Gokhale^{1*}, Russell K. Sam¹, Kim Somfleth¹, Matthew G. Thompson², Daphnée M. Marciniak³, Julian R. Smith¹, Emmanuelle Genoyer¹, Julie Eggenberger¹, Lan H. Chu¹, Moonhee Park², Steve Dvorkin¹, Andrew Oberst¹, Stacy M. Horner^{2,4}, Shao-En Ong³, Michael Gale Jr.^{1,5†}, Ram Savan^{1*}

Antiviral signaling downstream of RIG-I-like receptors (RLRs) proceeds through a multi-protein complex organized around the adaptor protein mitochondrial antiviral signaling protein (MAVS). Protein complex function can be modulated by RNA molecules that provide allosteric regulation or act as molecular guides or scaffolds. We hypothesized that RNA plays a role in organizing MAVS signaling platforms. We found that MAVS, through its central intrinsically disordered domain, directly interacted with the 3' untranslated regions of cellular messenger RNAs. Elimination of RNA by ribonuclease treatment disrupted the MAVS signalosome, including RNA-modulated MAVS interactors that regulate RLR signaling and viral restriction, and inhibited phosphorylation of transcription factors that induce interferons. This work uncovered a function for cellular RNA in promoting signaling through MAVS and highlights generalizable principles of RNA regulatory control of immune signaling complexes.

Innate immunity against RNA viruses is initiated when sentinel proteins, such as those in the RIG-I-like receptor (RLR) family, sense viral RNA motifs to induce type I and III interferons (IFNs), proinflammatory cytokines, and cellular defense genes, which establish an antiviral state (1, 2). Although a robust antiviral response is necessary to restrict viral infection, its aberrant induction can lead to inflammation and autoimmune disorders (3). Therefore, antiviral immune signaling needs to be tightly controlled for effective defense against viruses while restricting tissue damage. Uncovering the principles by which antiviral signaling is regulated is important for developing therapeutic strategies against both viral infection and inflammatory disorders.

Upon sensing viral RNA in the cytosol, the RLRs RIG-I and MDA5 translocate to the endoplasmic reticulum (ER)-mitochondria and other organelar contact sites, where they trigger the oligomerization of the adaptor protein, mitochondrial antiviral signaling protein (MAVS) (4–7). Oligomerized MAVS acts as a platform to recruit multiple proteins, which together organize into a higher-order signaling complex (termed the MAVS signalosome). At the MAVS signalosome, the kinases TBK1 and

IKK-ε and the IκB complex phosphorylate and activate the transcription factors interferon regulatory factor 3 (IRF3) and nuclear factor κB (NF-κB) (8–13), which then induce IFNs and an antiviral gene program. The MAVS signalosome requires a series of protein-protein interactions and posttranslational modifications (PTMs) at specific subcellular sites for efficient signal transduction (1, 14).

The number of proteins that have been shown to interact with RNA has greatly increased through recent proteomics-based studies (15, 16). RNA can interact with proteins in a sequence- and structure-dependent fashion; this ability is a key factor that drives the versatile functions of RNA, which extend well beyond its role as an intermediate between DNA and protein. RNA can recruit proteins and promote their interactions within molecular complexes. This is exemplified by ribosomal RNAs, which serve as a scaffold for dozens of interacting proteins to build the ribosome (17). Long non-coding RNAs and the 3' untranslated regions (UTRs) of mRNAs can similarly modulate protein and protein complex functions by serving as molecular guides or scaffolds (18–22). Further, RNA binding can lead to conformational or functional changes in proteins, thereby allosterically influencing their function in signaling and cell biological processes (23–28). However, a large proportion of proteins that have been shown to bind RNA do not contain any canonical RNA-binding domains (15, 16, 29, 30). This highlights the possibility of widespread RNA-mediated regulation of macromolecular protein complexes and their function. Therefore, we hypothesized that nonviral RNA could interact with proteins in the RLR-MAVS pathway to modulate signaling.

Results

Cellular RNA promotes IRF3 phosphorylation by the MAVS signalosome

As higher-order protein complexes can be scaffolded by RNA, we hypothesized that RNA may regulate MAVS signalosome activity. The phosphorylation of the transcription factor IRF3, which is required to induce IFNs and other target genes, is a key outcome of the activation of the RLR pathway through the MAVS signalosome (11–13, 31). To determine whether the MAVS signalosome is regulated by RNA, we tested its ability to phosphorylate IRF3 in vitro with or without ribonuclease (RNase) treatment (32). Here, we treated mitochondrial extracts from unstimulated or stimulated human embryonic kidney 293T (herein referred to as 293T) IRF3-knockout (IRF3^{KO}) cells with RNase and incubated them with cytosolic extract from unstimulated wild-type 293T (293T^{WT}) cells (Fig. 1A and fig. S1, A and B). 293T^{WT} cytosolic extract was the only source of IRF3 in these reactions, allowing for the discrimination of in vitro phosphorylated IRF3 as a measure of MAVS signalosome activity.

Mitochondrial extracts from 293T IRF3^{KO} cells infected with Sendai virus [SenV; a potent activator of RIG-I (4, 33)] but not from uninfected cells robustly phosphorylated IRF3 at serine 386. However, IRF3 phosphorylation by mitochondrial extracts from SenV-infected cells was inhibited by RNase treatment, which indicated that RNA promoted MAVS signalosome activity (Fig. 1, B and C). For these experiments, we used a cocktail of RNase A and RNase III (RNase A+III), which cleave single-stranded and double-stranded RNA, respectively. To further investigate which form of RNA promoted in vitro IRF3 phosphorylation by the MAVS signalosome, we compared this cocktail of RNases with treatment with RNase A or RNase III alone and with deoxyribonuclease (DNase) I treatment (fig. S1, C and D). RNase A treatment inhibited IRF3 phosphorylation to the same level as RNase A+III treatment. Conversely, neither RNase III alone nor DNase I treatment inhibited IRF3 phosphorylation. These data suggested that single-stranded RNAs or RNA regions were responsible for promoting MAVS signalosome function.

Although SenV RNA that is located within ribonucleoprotein complexes inside cells is resistant to RNase treatment (34), viral RNA complexed with RIG-I may still contribute to the observed RNA-modulated phosphorylation of IRF3 by the MAVS signalosome. To generate a system for measuring MAVS signalosome activity independently of viral RNA, we fused the N-terminal caspase activation and recruitment domains (CARDs) of RIG-I to FKBP12^{F36V} (F36V, Phe³⁶Val mutation) dimerizing domains (3xFV-N-RIG) (35, 36). Here, the small non-RNA molecule B/B multimerizes 3xFV-N-RIG, which was sufficient to activate the MAVS signalosome

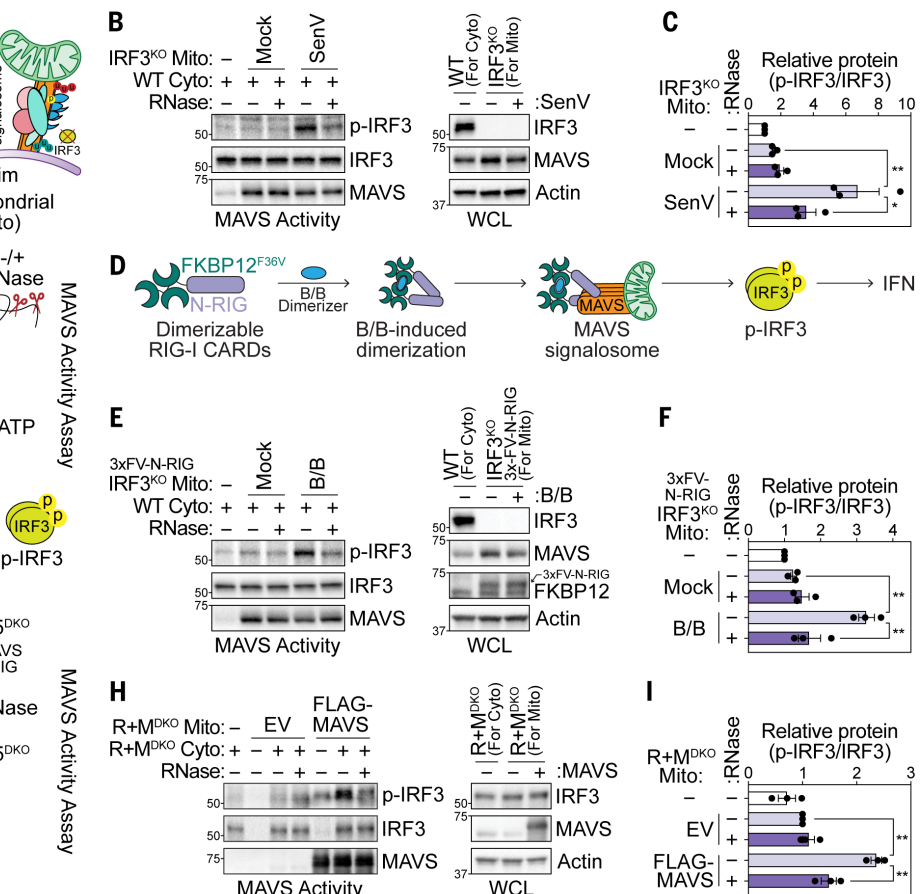
¹Department of Immunology, University of Washington, Seattle, WA. ²Department of Integrative Immunobiology, Duke University, Durham, NC. ³Department of Pharmacology, University of Washington, Seattle, WA. ⁴Department of Medicine, Duke University, Durham NC. ⁵Center for Innate Immunity and Immune Disease, University of Washington, Seattle, WA.

*Corresponding author. Email: ngokhale@uw.edu (N.S.G.); savanram@uw.edu (R.S.)

†Present address: Department of Microbiology and Immunology, University of Minnesota, Minneapolis, MN.

Fig. 1. Cellular RNA promotes IRF3 phosphorylation at the MAVS signalosome. (A) MAVS activity assay for in vitro IRF3 phosphorylation. Crude mitochondrial extracts (Mito) from 293T IRF3^{KO} cells are incubated with cytosolic extracts (Cyo) from unstimulated 293T^{WT} cells in the presence of ATP. IRF3 phosphorylation is analyzed by immunoblot. p-IRF3, phosphorylated IRF3. (B) MAVS activity assay to analyze in vitro IRF3 phosphorylation by mitochondrial extracts ± RNase treatment from mock or SenV-infected (100 HAU/mL, 16 hpi) 293T IRF3^{KO} cells. WCL, whole-cell lysates. (C) Quantification of p-IRF3 (Ser³⁸⁶) relative to IRF3 from experiments in (B). (D) Outline of the 3xFV-N-RIG system that activates the MAVS signalosome in the absence of viral RNA. FKBP12^{F36V} dimerization domains are fused to the N-terminal CARDs of RIG-I. Treatment with the small molecule B/B multimerizes 3xFV-N-RIG to activate downstream signaling. (E) MAVS activity assay to analyze in vitro IRF3 phosphorylation by mitochondrial extracts ± RNase treatment from mock or B/B-treated (10 nM, 3 hpt) 293T IRF3^{KO} cells stably expressing 3xFV-N-RIG. (F) Quantification of p-IRF3 relative to IRF3 (Ser³⁸⁶) from experiments in (E). (G) MAVS activity assay by extracts from RIG-I+MDA5^{DKO} (R+M^{DKO}) cells. (H) MAVS activity assay to analyze in vitro IRF3 phosphorylation by mitochondrial extracts ± RNase treatment from empty vector (EV)- or FLAG-MAVS-transfected (10 μg, 48 hpi) 293T R+M^{DKO} cells using cytosolic extract from unstimulated 293T R+M^{DKO}. (I) Quantification of p-IRF3 (Ser³⁸⁶) relative to IRF3 from experiments in (H). Data in (B), (E), and (H) are representative of three biological replicates. Bar graphs in (C), (F), and (I) show the mean ± SEM of three biological replicates, and data points represent values from individual replicates. *P ≤ 0.05; **P ≤ 0.01; ***P ≤ 0.001; one-way ANOVA with Tukey's multiple comparison test.

and propagate downstream signaling (Fig. 1D). B/B treatment rapidly induced *IFNβ* in 293T cells stably expressing 3xFV-N-RIG, but not in 293T^{WT} cells (fig. S1E). To test whether RNase treatment inhibited IRF3 phosphorylation in the absence of an activating nonself RNA ligand, we performed the MAVS activity assay in 293T IRF3^{KO} cells that stably expressed 3xFV-N-RIG. Although mitochondrial extracts from B/B-treated cells phosphorylated IRF3 in vitro, RNase treatment of these extracts abolished IRF3 phosphorylation (Fig. 1, E and F). To confirm that cellular RNAs bound to RIG-I or MDA5 were not responsible for these phenotypes, we incubated mitochondrial extracts from stimulated and unstimulated 293T cells deleted for RIG-I and MDA5 (R+M^{DKO}) with cytosolic extract from unstimulated 293T R+M^{DKO} cells. Here, the MAVS signalosome was activated either by MAVS overexpression, which is sufficient to drive signaling, or by B/B treatment of cells expressing 3xFV-N-RIG (Fig. 1G and fig. S1, F and G). IRF3 phosphorylation by mitochon-



drial extracts from both MAVS-overexpressing or B/B-treated cells was inhibited by RNase treatment (Fig. 1, H and I and fig. S1, H and I).

The MAVS signalosome activates NF-κB in addition to IRF3 (8, 32). To test whether RNA also promoted the phosphorylation of NF-κB downstream of MAVS, we incubated mitochondrial extracts from SenV-infected 293T^{WT} cells with cytosolic extract from uninfected cells and analyzed phosphorylation of NF-κB p65. Mitochondrial extracts from SenV-infected cells subtly phosphorylated p65 in vitro compared with those from uninfected cells. However, this phosphorylation was abolished by RNase treatment (fig. S1, J and K). Together, these data confirmed that cellular RNA promoted MAVS signalosome activity at the level of IRF3 and NF-κB activation.

The MAVS signalosome is associated with cellular RNA

Given that cellular RNA regulates antiviral signaling through MAVS, we hypothesized that

MAVS and its signalosome interacted with RNA. RNA association with proteins and protein complexes can be determined by a RNase-dependent shift in their migration through a sucrose gradient (37). Owing to the higher mass conferred by bound RNA, proteins associated with RNA are found in higher sucrose (denser) fractions in the absence of RNase and migrate to lower sucrose (less dense) fractions in the presence of RNase (Fig. 2A). To test whether MAVS exhibits an RNase-dependent shift, we treated mitochondrial lysates from uninfected and SenV-infected 293T cells with RNases then separated the lysates by ultracentrifugation through sucrose gradients and measured the migration of MAVS signalosome proteins by immunoblotting of collected fractions. Corroborating previous work (7, 38), SenV infection caused MAVS to migrate to heavy fraction 10 owing to its oligomerization and the formation of the MAVS signalosome (Fig. 2, B and C). Heavy but not light fractions led to in vitro phosphorylated IRF3 when incubated with

Fig. 2. The MAVS signalosome is associated with cellular RNA.

(A) RNase-dependent shift assay to identify RNA-associated proteins. Mitochondrial lysates treated with RNase inhibitor ($-$ RNase) or an RNase cocktail ($+R$ Nase) are separated on a sucrose gradient by ultracentrifugation. RNA-associated proteins have reduced migration to heavy fractions in the presence of RNase. **(B)** Immunoblot analysis of fractions collected after sucrose gradient ultracentrifugation of mitochondrial lysates \pm RNase treatment from mock- and SenV-infected (100 HAU/mL, 14 hpi) 293T cells. **(C)** Quantification of the indicated protein in fraction 10 relative to that in fraction 3 from experiments in (B). **(D)** Immunoblot analysis of fractions collected after sucrose gradient ultracentrifugation of mitochondrial lysates \pm RNase treatment from 293T cells transfected with empty vector (EV) and FLAG-tagged MAVS (10 μ g, 24 hpt). **(E)** Quantification of the indicated protein in fraction 10 relative to that in fraction 3 from experiments in (D). **(F)** Immunoblot analysis of fractions collected after sucrose gradient ultracentrifugation of mitochondrial lysates \pm RNase treatment from 293T R+M^{DKO} cells transfected with FLAG-tagged MAVS (10 μ g, 24 hpt). **(G)** Quantification of MAVS in fraction 10 relative to that in fraction 3 from experiments in (F).

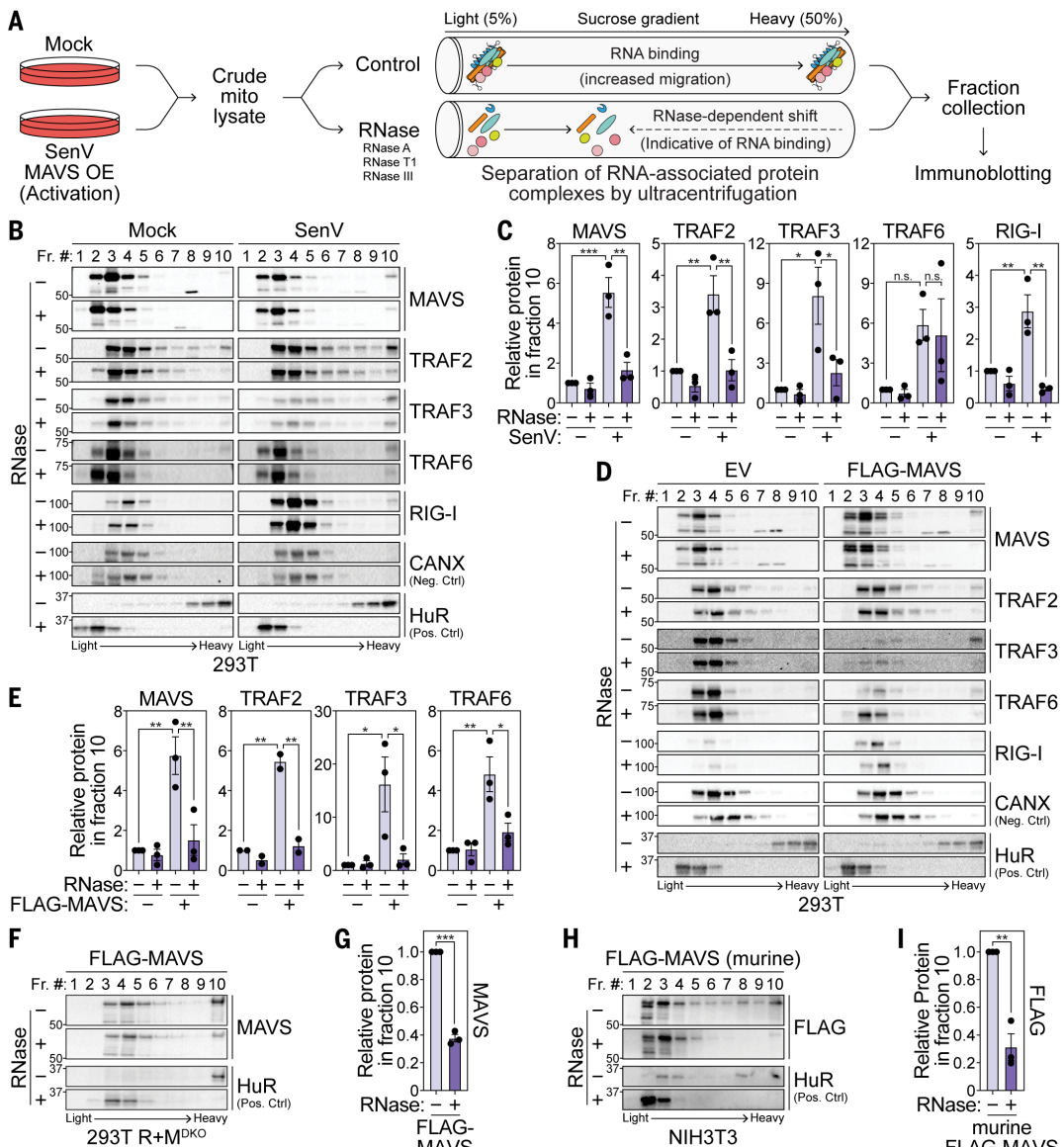
(H) Immunoblot analysis of fractions collected after sucrose gradient ultracentrifugation of mitochondrial lysates \pm RNase treatment from murine NIH3T3 cells transfected with FLAG-tagged murine MAVS (10 μ g, 24 hpt). **(I)** Quantification of FLAG-tagged murine MAVS in fraction 10 relative to that in fraction 3 from experiments in (H). Data in (B), (D), (F), and (H) are representative of three biological replicates. Bar graphs in (C), (E), (G), and (I) show the mean \pm SEM of three biological replicates, and data points represent values from individual replicates. * $P \leq 0.05$; ** $P \leq 0.01$; *** $P \leq 0.001$; one-way ANOVA with Tukey's multiple comparison test [(C) and (E)] or unpaired t test [(G) and (I)].

cytosolic extracts, which indicated that the MAVS signalosome migrated to heavy fraction 10 (fig. S2A). RNase treatment reduced MAVS migration to fraction 10, just as it did for the canonical RNA binding protein (RBP), HuR (Fig. 2, B and C). Additionally, RNase treatment reduced the cosedimentation of key components of the MAVS signalosome, including TNF receptor-associated factor 2 (TRAF2) and TRAF3, at heavy fractions with MAVS during SenV infection, indicating that the mass of the entire complex was reduced by RNase treatment and that one or more of the proteins in the MAVS signalosome were associated with RNA. Given

that RIG-I interacts with SenV RNA (39), the RNase-dependent shift for this sensor is expected in infected cells. Migration of CANX, a protein not known to interact with RNA, was unaffected by RNase treatment in these experiments. Encephalomyocarditis virus (EMCV) preferentially activates MDA5 as opposed to RIG-I (4), and we observed a similar RNase-dependent shift for MAVS in cells infected with EMCV (fig. S2, B and C).

MAVS overexpression is sufficient to drive downstream signaling in the absence of viral infection. MAVS, TRAF2, TRAF3, and TRAF6 also demonstrated an RNase-dependent shift

following overexpression of FLAG-tagged MAVS (Fig. 2, D and E). However, RIG-I did not cosediment with MAVS in the heavy fraction during MAVS overexpression likely because of the absence of interacting viral RNA, suggesting that viral RNA bound to RIG-I was not responsible for the RNase-dependent shift of MAVS signalosome components. MAVS also had an RNase-dependent shift when overexpressed in 293T R+M^{DKO} cells (Fig. 2, F and G). Similarly, MAVS demonstrated an RNase-dependent shift in 293T RIG-I^{KO} and 293T R+M^{DKO} cells transfected with the N-terminal domains of RIG-I or MDA5 (36), respectively,



which activate signaling but do not interact with RNA (fig. S2, D and H). FLAG-tagged murine MAVS overexpressed in mouse NIH 3T3 cells also exhibited an RNase-dependent shift, demonstrating that MAVS-RNA association is conserved between human and murine cells (Fig. 2, H and I). Together, these data demonstrated that higher-order MAVS complexes were abolished by RNase treatment, indicating that the MAVS signalosome was associated with cellular RNA independently of RIG-I or MDA5.

MAVS oligomerization also increases the migration of this protein to higher sucrose fractions (7, 38). To ensure that the RNase-dependent shift of the MAVS signalosome was not due to a resolution of MAVS oligomers, we tracked protein oligomers using semidenaturing detergent agarose gel electrophoresis (SDD-AGE) on mitochondrial lysates isolated from uninfected

or SenV-infected 293T cells with or without RNase treatment. SenV infection led to the formation of MAVS oligomers, which were not resolved by RNase treatment, although β -mercaptoethanol (β -ME) resolved MAVS oligomers as expected (fig. S2I). Similarly, oligomers formed by MAVS overexpression were resolved by β -ME but were refractory to RNase treatment (fig. S2J). Therefore, we concluded that the observed RNase-dependent shift of the MAVS signalosome was due to RNA association rather than MAVS deoligomerization.

MAVS interacts with cellular RNA through its conserved central disordered domain

Infrared dye crosslinking and immunoprecipitation (irCLIP) allows for the detection of RNA-protein complexes (40). Following stringent immunoprecipitation of the target protein, an

infrared dye fluorescent oligonucleotide was ligated to ultraviolet (UV)-crosslinked RNA fragments, and RNA-protein complexes were visualized by SDS-polyacrylamide gel electrophoresis (PAGE) (Fig. 3A and fig. S3A). To test whether MAVS interacted with RNA directly, we performed irCLIP on FLAG-tagged MAVS expressed in 293T MAVS^{KO} cells and detected crosslinking-dependent MAVS-RNA complexes (Fig. 3, B and C, and fig. S3, A and B). irCLIP of endogenous MAVS in uninfected and SenV-infected 293T^{WT} and 293T R+M^{DKO} cells revealed that MAVS interacted with RNA in both uninfected and infected cells and that this interaction is independent of RIG-I and MDA5 (Fig. 3, D and E, and fig. S3, C and D). Endogenous MAVS also interacted with RNA in primary human monocyte-derived macrophages (Fig. 3, F and G). Further, we found that

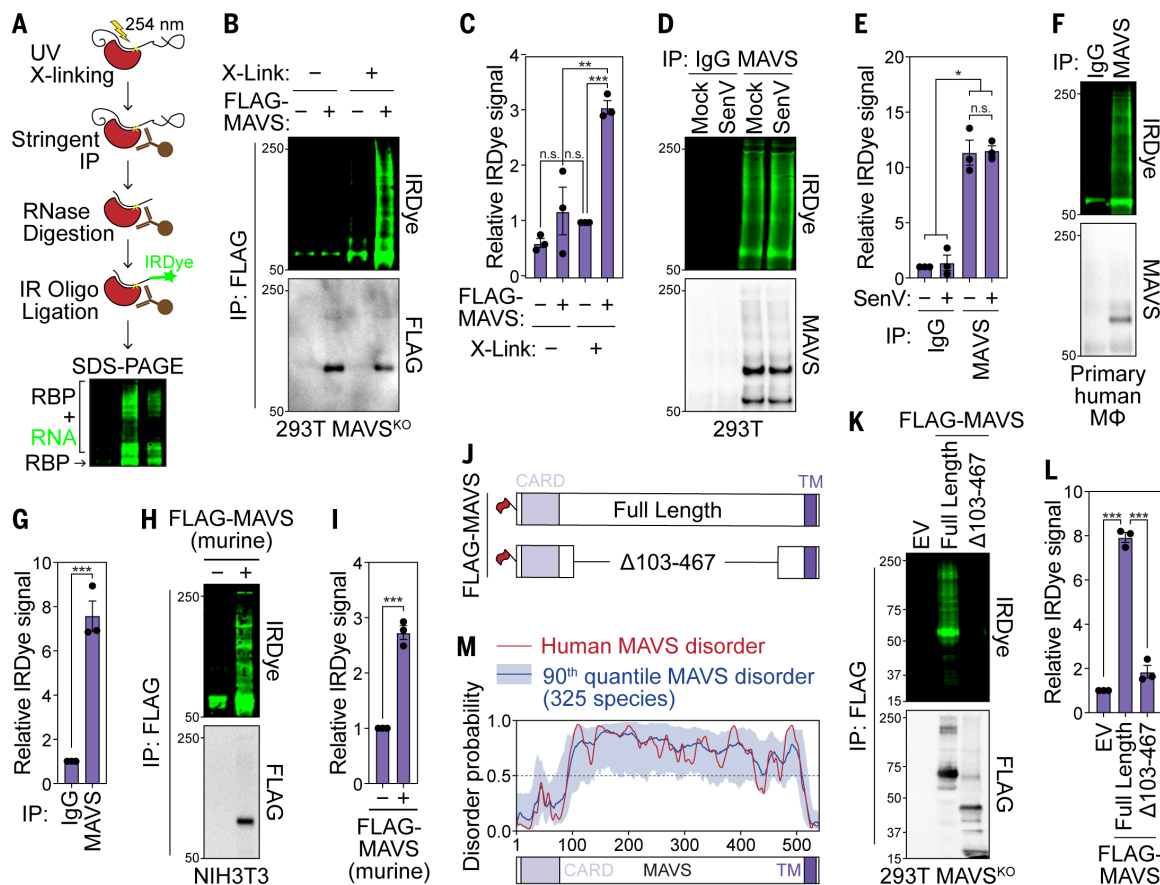


Fig. 3. MAVS interacts with RNA through its central intrinsically disordered region.

Region. (A) irCLIP strategy to visualize RNA-protein complexes. The protein of interest is stringently immunoprecipitated, and UV-crosslinked RNA is digested into fragments with RNase A. After ligating an IRDye-800-conjugated oligonucleotide, complexes are resolved by SDS-PAGE. RNA-protein complexes are detected by IRDye-800 fluorescence, and immunoprecipitation (IP) is validated by immunoblot analysis. UV crosslinking, UV X-linking. (B) irCLIP ± crosslinking of FLAG-tagged MAVS expressed in 293T MAVS^{KO} cells (24 hpt). (C) Quantification of IRDye signal in experiments in (B). (D) irCLIP of endogenous MAVS from mock- and SenV-infected (100 HAU/mL, 16 hpi) 293T cells. (E) Quantification of IRDye signal in experiments in (D). (F) irCLIP of endogenous MAVS from naïve primary human monocyte-derived

macrophages (M ϕ). (G) Quantification of IRDye signal in experiments in (F). (H) irCLIP of FLAG-tagged murine MAVS expressed in murine NIH3T3 cells (24 hpt). (I) Quantification of IRDye signal in experiments in (F). (J) Schematic of FLAG-tagged full-length MAVS and MAVS Δ 103-467 used in (L). (K) irCLIP of the indicated FLAG-tagged MAVS constructs expressed in 293T MAVS^{KO} cells (24 hpt). (L) Quantification of IRDye signal in experiments in (L). (M) Prediction of disorder in human MAVS (red) and in 325 mammalian species (blue) by using IUPred3. Data in (B), (D), (F), (H), and (K) are representative of three biological replicates. Bar graphs in (C), (E), (G), (I), and (L) are the mean \pm SEM of three biological replicates, and data points represent values from individual replicates. *P \leq 0.05; **P \leq 0.01; ***P \leq 0.001 by one-way ANOVA with Tukey's multiple comparison test [(C), (E), and (L)] or unpaired t test [(G) and (I)].

overexpressed FLAG-tagged murine MAVS interacted with RNA in mouse NIH3T3 cells, suggesting that MAVS-RNA interaction was conserved between humans and mice (Fig. 3, H and I).

To identify the domains of MAVS responsible for interacting with RNA, we performed irCLIP in 293T MAVS^{KO} cells by expressing FLAG-tagged human MAVS constructs with deletions in the caspase activation and recruitment domain (CARD), transmembrane domain (TM), or the central region between amino acids 103 and 467 (fig. S3E). The CARD is required for MAVS oligomerization and activation, whereas the TM domain mediates MAVS localization to mitochondrial and other cellular membranes (12, 14). The central region of MAVS between amino acids 103 and 467 harbors binding sites for many MAVS-interacting proteins, including TRAF2, TRAF3, TRAF6, and IRF3 (8, 10, 14, 41). Overexpression of these mutants in 293T MAVS^{KO} cells did not induce signaling (fig. S3F). Deletion of the CARD, TM, or both CARD and TM did not reduce MAVS-RNA interaction as determined by irCLIP (fig. S3, G and H). However, deletion of amino acids 103 to 467 of MAVS eliminated the ability of this protein to bind RNA, which indicated that MAVS interacted with RNA through this region (Fig. 3, J to L, and fig. S3, G and H). The MAVS central region was sufficient for RNA binding because a MAVS construct encoding only amino acids 103 to 467 interacted with RNA (fig. S3, I to K). We also tested the ability of N-terminally truncated MAVS proteoforms that derived from alternative translation initiation by irCLIP analysis of FLAG-tagged proteoforms (38, 42). MAVS proteoforms initiating at Met¹⁴², Met³⁰³, and Met³⁶⁷ still interacted with RNA. However, the Met⁴⁴⁹ proteoform, which retains only 18 amino acids of the central region, did not bind RNA, highlighting the role of this MAVS central region in RNA interaction (fig. S3, L to N).

The central region of MAVS is predicted to harbor extensive intrinsic disorder by two different prediction software packages, IUPred3 (43) and FuzPred (44), as well as AlphaFold (45), and is enriched for disorder-promoting residues, such as serine, proline, and glycine (Fig. 3M and fig. S3, O to Q). Further, this disorder across the central region of MAVS was predicted to be conserved across 325 species (Fig. 3M). Intrinsically disordered domains are known to promote protein-RNA interactions (16, 29, 30, 46–48). Together, these data indicate that MAVS directly interacted with RNA through its conserved, central disordered domain.

MAVS interacts with the 3'UTR of mRNAs

Traditional UV crosslinking- and immunoprecipitation-based techniques to identify bound RNAs are challenging for proteins that lack canonical RNA-binding domains, such as MAVS

(49, 50). Therefore, we used targeted RNA editing mediated by APOBEC1 to identify MAVS-associated RNAs. Here, MAVS is fused to APOBEC1, which catalyzes cytosine-to-uracil transitions in proximal RNAs. These transitions can be detected by RNA sequencing without relying on crosslinking or immunoprecipitation (51, 52).

To profile MAVS-associated RNAs, we fused FLAG-tagged APOBEC1 to the N terminus of full-length MAVS (APOBEC1-MAVS^{FL}). We used FLAG-APOBEC1 as a background control (CTRL) and FLAG-APOBEC1 fused to the C-terminal transmembrane helix of MAVS (MAVS^{C-term}) as a mitochondrially localized background control to account for off-target editing within the subcellular vicinity of MAVS (Fig. 4A). Transfection of APOBEC1-MAVS^{FL} into 293T cells induced *IFNB1*, indicating that this construct can form the MAVS signalosome, whereas APOBEC1 and APOBEC1-MAVS^{C-term} did not induce *IFNB1* (fig. S4, A and B). Further, although APOBEC1 was localized primarily to the cytoplasm, both APOBEC1-MAVS^{FL} and APOBEC1-MAVS^{C-term} had a similar membrane-associated pattern of localization (fig. S4C).

RNA sequencing data from 293T cells transfected with these constructs were analyzed by using the Bullseye pipeline (52, 53) to identify RNAs with increased cytosine-to-thymine editing with APOBEC1-MAVS^{FL} as compared to controls. We identified enhanced cytosine-to-thymine editing at a set of 167 sites in 107 transcripts when comparing APOBEC1-MAVS^{FL} to both controls together, and further editing sites emerged when comparing APOBEC1-MAVS^{FL} to each control individually (Fig. 4B and data S1). The low overlap of edited transcripts between APOBEC1-MAVS^{FL} and APOBEC1-MAVS^{C-term} when compared with APOBEC1 and the higher number of transcripts modified by APOBEC1-MAVS^{FL} indicated that APOBEC1-MAVS^{FL} specifically edits MAVS-associated transcripts (Fig. 4B and fig. S4D). Most editing sites (86%) were identified in the 3'UTRs of mRNAs.

Given that MAVS interacted with more than 100 mRNAs, it seemed unlikely that one transcript would be a primary driver of RNA-regulated modulation of MAVS function. However, the 3'UTRs of *PMAIP1* and *IFIT2*, which contained 9 and 23 editing sites, respectively, suggested that these UTRs are highly associated with MAVS (Fig. 4C and fig. S4E). The rate of editing of called sites in *PMAIP1* by APOBEC1-MAVS^{FL} was corroborated by Sanger sequencing (fig. S4, F and G). *PMAIP1* and *IFIT2* binding to MAVS was further validated by CLIP-reverse transcription quantitative polymerase chain reaction (RT-qPCR). Both transcripts were enriched with full-length FLAG-MAVS and FLAG-MAVS Δ1–102, which retained the RNA binding central region of MAVS, as compared with the non-RNA binding FLAG-MAVS Δ103–467 when these constructs were overexpressed in 293T

MAVS^{KO} cells (Fig. 4, D and E). Both *PMAIP1* and *IFIT2* are induced by IFNs (54), and this was evident by their increased expression in the presence of MAVS^{FL} in the RNA sequencing data (Fig. 4C). This may indicate a feedback mechanism, wherein some nascent, newly transcribed, IFN-inducible mRNAs bind to MAVS. Indeed, CLIP-RT-qPCR, when normalized to input RNA levels, indicated that the interaction of endogenous MAVS with *PMAIP1* and *IFIT2* mRNAs was augmented by SenV infection (Fig. 4F). Taken together, these data suggested that MAVS interacted primarily with the 3'UTRs of cellular RNAs and that specific MAVS-RNA interactions may be altered during active signaling and involved in feedback regulation.

RNA modulates functional MAVS protein-protein interactions

Because MAVS interacted with RNA and RNase treatment inhibited in vitro IRF3 phosphorylation by the MAVS signalosome, we hypothesized that RNA altered the ability of MAVS to interact with proteins required for proper signaling. To identify proteins that differentially interact with MAVS in an RNA-dependent manner, we immunoprecipitated (immunoprecipitation, IP) FLAG-MAVS from mitochondrial lysates of transfected 293T cells with or without RNase treatment and analyzed immunoprecipitated MAVS complexes by mass spectrometry (MS) (Fig. 5A). Mitochondrial lysates from empty vector-transfected cells without RNase treatment were used as background controls.

We identified a total of 3200 proteins across five biological replicates, 1094 of which were enriched (\geq twofold, $P \leq 0.05$, detected in <30% of datasets in the CRAPome database) with FLAG-MAVS ± RNase treatment over empty vector control (Fig. 5B, fig. S5A, and data S2). These included proteins known to interact with MAVS and regulate its function, such as core signalosome components, such as TRAF2, TRAF3, TRAF6, and TBK1, highlighting the specificity of this IP-MS strategy (8, 10, 14, 55). Functional network analysis with STRING (56) revealed that many MAVS-interacting proteins fell into discrete protein complexes or functional categories (fig. S5B). Gene set enrichment analysis (57, 58) further revealed that these proteins were enriched in pathways related to immune responses, signaling cascades, metabolism, organellar organization, transport, ER stress, and posttranslational modification (fig. S5C).

Most MAVS-interacting proteins were similarly enriched with or without RNase treatment. However, nine proteins had decreased, and 25 had increased ($\log_2FC > |0.5|$; FC, fold change) interaction with MAVS following RNase treatment (Fig. 5B and fig. S5D). Proteins with reduced MAVS interaction upon RNase treatment had a higher RBP2GO score on average, indicating that these proteins were more likely

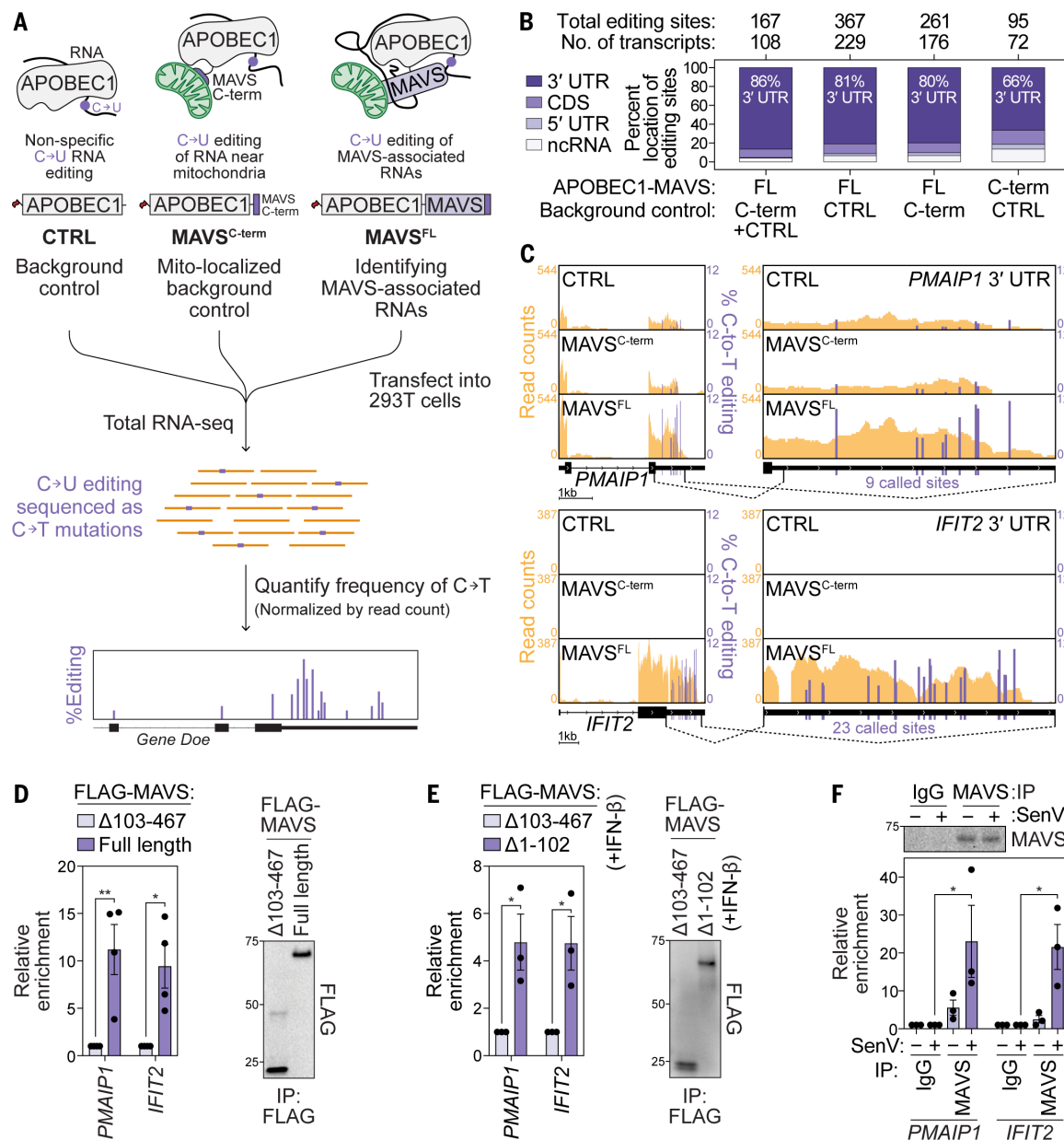


Fig. 4. MAVS interacts with the 3'UTRs of mRNAs. (A) Targeted APOBEC1-mediated editing approach used to profile MAVS-interacting RNAs. Cytosine-to-thymine edits in sequenced cDNA enhanced with APOBEC1-MAVS^{FL} overexpression relative to nonspecific (APOBEC1 alone; control) and mitochondria-localized (APOBEC1-MAVS^{C-term}) background controls identifies MAVS-associated RNAs. C, cytosine; T, thymine; U, uracil. (B) Summary of cytosine-to-thymine editing sites and edited transcripts identified when comparing the indicated APOBEC1-MAVS constructs with background controls across biological triplicates. (C) Percent cytosine-to-thymine editing (purple) at called sites in *PMAIP1* and *IFIT2* 3'UTRs (mean of three replicates). Read counts from one representative experiment are shown in yellow. Scale bars represent 1 kb of genome length. (D) (Left) CLIP-RT-qPCR analysis of normalized enrichment relative to input of *PMAIP1* and *IFIT2* mRNA by immunoprecipitation of the indicated FLAG-tagged MAVS constructs in transfected

293T MAVS^{KO} cells (24 hpt). (Right) Representative immunoblot of immunoprecipitated fractions. (E) (Left) CLIP-RT-qPCR analysis of normalized enrichment relative to input of *PMAIP1* and *IFIT2* mRNA by immunoprecipitation of the indicated FLAG-tagged MAVS constructs in transfected 293T MAVS^{KO} cells (16 hours) and treated with IFN-β (100 U/mL, 24 hours). (Right) Representative immunoblot of immunoprecipitated fractions. (F) (Bottom) CLIP-RT-qPCR analysis of normalized enrichment relative to input of *PMAIP1* and *IFIT2* mRNA by immunoprecipitation of endogenous MAVS from mock- and SenV-infected (100 HAU/ml, 16 hpt) 293T cells. IgG was used as background control. (Top) Representative immunoblot of immunoprecipitated fractions. Bar graphs are the mean ± SEM of four (D) or three [(E) and (F)] biological replicates and data points represent values from individual replicates. *P ≤ 0.05; **P ≤ 0.01; unpaired t test [(D) and (E)] or one-way ANOVA with Tukey's multiple comparison test (F).

to interact with RNA (fig. S5D). The RBP2GO score is calculated based on a protein's interaction networks with other RBPs and the number of times it is identified in proteomic RBP

discovery datasets (15). On the other hand, proteins with increased MAVS interaction upon RNase treatment had a lower RBP2GO score on average.

To identify whether these RNA-altered MAVS interactors regulated RLR signaling, we performed a targeted small interfering RNA (siRNA) screen in 293T cells stably expressing an *IFNB1^{2X-Gaussia}*

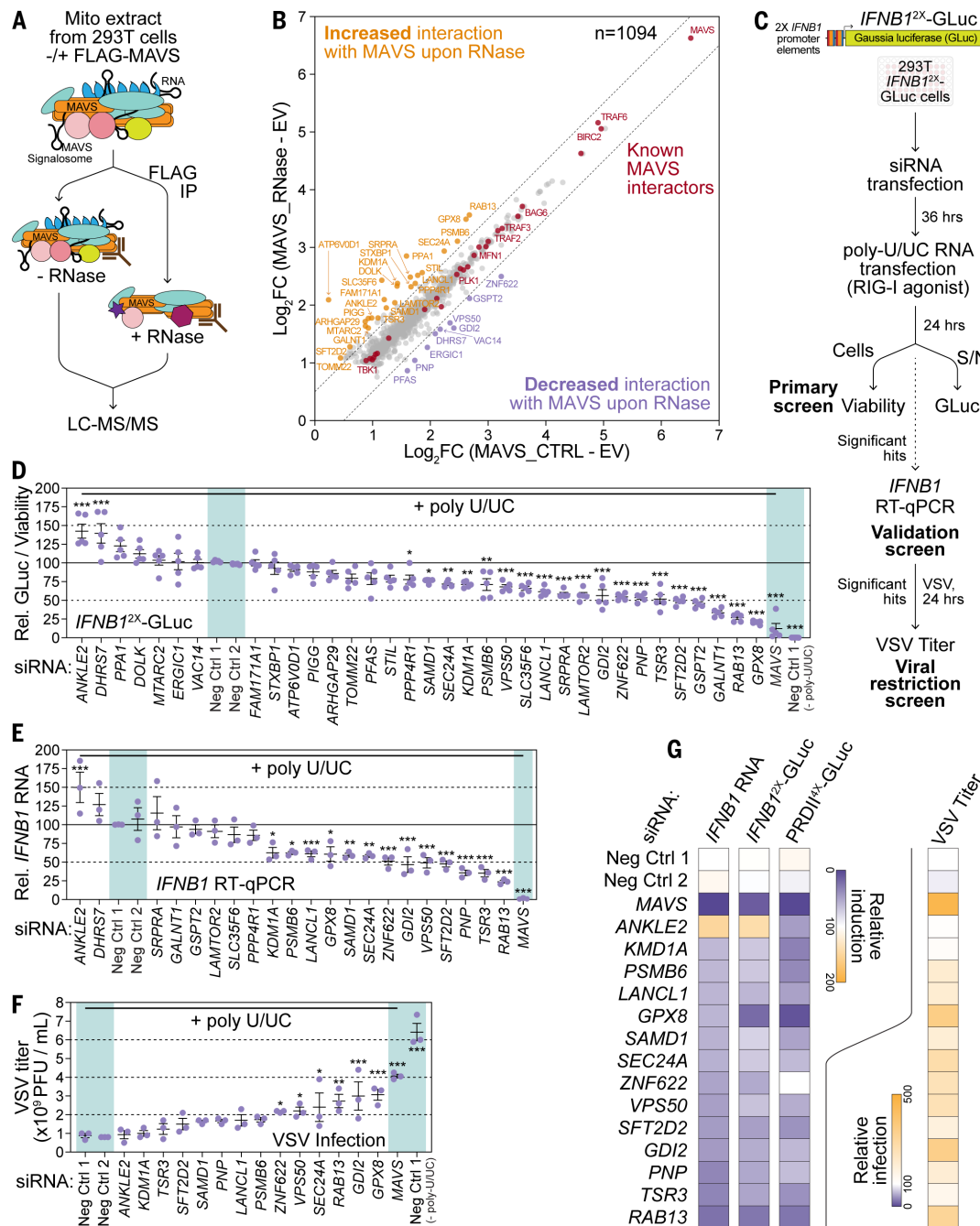


Fig. 5. RNA alters functional protein-protein interactions at the MAVS signalosome. (A) Immunoprecipitation and mass spectrometry strategy to identify RNA-dependent MAVS interactors. (B) Scatterplot of 1094 proteins significantly enriched with MAVS ($\log_2 \text{FC} \geq 2$, $P \leq 0.05$, found in <30% of CRAPome datasets) ± RNase over empty vector control across five biological replicates. Dashed lines delineate $|\log_2 \text{FC}| = 0.5$ from the diagonal. Known MAVS-interacting proteins are in red, those with decreased MAVS-interaction upon RNase treatment are in purple, and those with increased MAVS-interaction upon RNase treatment are in ochre. (C) Schematic of primary and validation siRNA screens for RNA-dependent MAVS interactors. (D) Relative GLuc activity normalized to viability following poly-U/UC RNA transfaction (50 ng, 24 hpt) in 293T *IFNB1^{2X}*-GLuc reporter cells upon depletion of the indicated factors by siRNA treatment (36 hours). Controls are highlighted in teal. (E) Normalized

IFNB1 mRNA expression relative to *HPRT1* following poly-U/UC RNA transfaction (50 ng, 24 hpt) in 293T cells upon depletion of the indicated factors by siRNA treatment (36 hours), determined by RT-qPCR. Controls are highlighted in teal. (F) Quantification of viral titers from the supernatants of 293T cells depleted for the indicated factors by siRNA (36 hours), transfected with low-dose poly-U/UC RNA (50 ng, 16 hours) and infected with VSV (MOI 0.001, 24 hours), as determined by plaque forming assay. Controls are highlighted in teal. (G) Summary of the effect of depletion of RNA-modulated MAVS interactors on *IFNB1* RNA (E), *IFNB1^{2X}*-GLuc (D), and *PRDII^{4X}*-GLuc (fig. S6J) induction as well viral restriction (F). Dot plots are the mean ± SEM of five (D) or three [(E) and (F)] biological replicates and data points represent values from individual replicates. * $P \leq 0.05$; ** $P \leq 0.01$; *** $P \leq 0.001$ by one-way ANOVA with Tukey's multiple comparison test.

luciferase (GLuc) reporter (Fig. 5C). Here, secreted GLuc, kept low under basal conditions by a destabilizing PEST domain, is induced by two tandem enhanceosome elements (59) from the *IFNB1* promoter (fig. S6A). Clonal 293T *IFNB1^{2X}*-GLuc cells demonstrate GLuc induction in response to an RLR ligand, such as transfected poly-U/UC (60), an in vitro-transcribed, immunogenic RNA fragment from the hepatitis C virus genome that potently activates RIG-I (fig. S6B). Further, GLuc induction upon poly-U/UC RNA transfection was inhibited by depletion of MAVS or IRF3, indicating that this reporter is sensitive to perturbation of the RLR pathway (fig. S6C).

Depletion of 20 out of 34 of the RNA-modulated MAVS-interacting proteins we identified affected *IFNB1* promoter-driven GLuc production in response to poly-U/UC RNA, with two increasing and 18 decreasing GLuc production (Fig. 5D and fig. S6D). To account for possible effects on GLuc transcription, translation, or secretion, we performed a secondary screen on hits that altered *IFNB1^{2X}*-GLuc production, testing for the induction of *IFNB1* mRNA by poly-U/UC transfection in 293T cells (Fig. 5E and fig. S6E). From these screens, we determined that depletion of four of the nine proteins with reduced interaction with MAVS upon RNase treatment (PNP, ZNF622, GDI2, and VPS50) decreased both GLuc and *IFNB1* induction, indicating that these factors promote signaling. On the other hand, we found that 9 of the 25 proteins with increased MAVS interaction upon RNase treatment (GPX8, RAB13, SFT2D2, TSR3, LANCL1, PSMB6, KDM1A, SEC24A, and SAMD1) also promote signaling, whereas ANKLE2 inhibits signaling (Fig. 5E).

Several of these RNA-modulated MAVS interactors cosedimented with MAVS during MAVS overexpression and demonstrated an RNase-dependent shift (fig. S6F). To test whether candidates that altered *IFNB1* expression also modulated NF-κB activation, we determined whether their depletion affected GLuc induction from a reporter driven by four PRDII NF-κB-binding elements (59) from the *IFNB1* promoter (fig. S6, G and H). Depletion of most targets reduced the induction of this reporter in 293T PRDII^{4X}-GLuc stable cells after poly-U/UC RNA transfection, showing high concordance with changes in *IFNB1* expression (Fig. S6I-J).

Lastly, we tested whether the impact of RNA-modulated MAVS interactors on *IFNB1* induction was important for viral restriction. We transfected a low dose of poly-U/UC RNA to induce IFN-β in 293T cells depleted for these factors, infected these cells with vesicular stomatitis virus (VSV), and then measured viral titer by plaque-forming assay. Depletion of GPX8, GDI2, RAB13, SEC24A, VSP50, and ZNF622, all of which promote *IFNB1* induction, increased viral titers, which indicated that these factors were required for maximal antiviral response

(Fig. 5, F and G). Together, these data demonstrated that proteins that associated with MAVS in a cellular RNA-regulated manner could modulate antiviral signaling through the RLR-MAVS pathway. To our knowledge, none of these factors have yet been found to play a role in RLR-MAVS signaling and instead represent previously unappreciated regulatory components of the MAVS signalosome.

Discussion

In this work, we uncovered a role for cellular RNA in promoting antiviral responses downstream of RLR signaling through interaction with the adaptor protein MAVS. We found that the MAVS signalosome associated with RNA and that MAVS directly bound to the 3'UTRs of cellular mRNAs through its central disordered domain. RNA binding altered the ability of MAVS to interact with several protein interactors, thereby modulating signaling and viral restriction. Therefore, IFN induction through the RLR pathway is initially triggered by pathogenic self- or nonself RNA but was also augmented by cellular RNA binding to MAVS.

Although MAVS does not harbor a canonical RNA-binding domain, we found that MAVS interacts with the UTRs of cellular mRNAs through its central disordered region. Disordered domains can directly interact with RNA, and a large proportion of proteins recognized to interact with RNA do not contain canonical RNA-binding domains but do encode disordered regions. Such interactions are common; approximately half of all peptides that can be crosslinked to RNA map to disordered regions (16, 30, 61). Typically, disordered RNA-binding domains are enriched in positively charged arginine- or lysine-rich patches or arginine-glycine and arginine-serine repeats, which encourage interaction with the negatively charged phosphate backbone of RNA (29, 30). Notably, the MAVS disordered region, which is enriched for conserved disorder-promoting amino acids, including glycine, serine, and proline, does not contain many positively charged residues, indicating non-canonical interaction with RNA. Uncovering the mode of this interaction will be important for determining the specificity of MAVS binding to the 3'UTRs of specific cellular RNAs. Some of these mRNAs are IFN inducible, which points to feedback regulation of antiviral signaling. Therefore, future work will also aim to identify the functions of specific transcripts in regulating the MAVS signalosome and whether the lengthening or shortening of 3'UTRs, a widespread feature of viral infection and immune activation, may further modulate MAVS-RNA interaction and function (62–64).

Previous studies have shown that protein-protein interactions form the MAVS signalosome, nucleated by CARD-mediated oligomerization of MAVS itself. These studies have revealed

critical effectors that are required for the activation of IFNs, such as TRAF2, TRAF3, TRAF6, TBK1, and ATP13A1, all of which we identified in our proteomics approach (8–10, 65, 66). Our study expands these functional interactors, as we uncovered proteins that associate with MAVS in an RNA-modulated manner to influence IFN induction and, consequently, antiviral restriction. Notably, we found both positive and negative regulators of MAVS activity, suggesting that activation of this pathway is tightly regulated at the adaptor level. We propose two potential mechanisms for how RNA could affect these protein-protein interactions with MAVS. Firstly, cellular RNA could coordinate protein-protein interactions directly. For example, RNA could simultaneously interact with MAVS and RNA-binding factors that promote signaling, such as ZNF622 and GDI2, thereby bringing these proteins into proximity for functional interaction. Similarly, RNA could sterically prevent interactions between MAVS and factors that inhibit signaling, such as ANKLE2, or change the temporal order of signalosome coalescence required for efficient signaling. Secondly, binding to RNA may change the conformation of the disordered region of MAVS, thereby promoting or inhibiting protein binding. Disordered regions are flexible and can undergo local disorder-to-order transitions upon ligand binding, which can stabilize and functionalize neighboring segments. For example, RNA binding changes the conformational state of the disordered N-terminal domain of MYC, thereby potentiating the formation of functional MYC complexes (26). Therefore, RNA-dependent conformational changes in MAVS may stabilize or destabilize short linear motifs within the conserved disordered region to modulate interactions with other signalosome components. Indeed, specific binding motifs for TRAF proteins and IRF3 within the MAVS disordered region are already known to be exposed and functionalized by CARD-mediated MAVS oligomerization (7, 41). Except for a few motifs in the disordered region, to which TRAF proteins and IRF3 bind, and previously discovered sites of MAVS posttranslational modification, the function of the evolutionarily conserved disordered region in MAVS has been unclear. Our study reveals that RNA binding to this disordered region adds an important regulatory layer to MAVS function and identifies accessory factors that influence antiviral signaling through MAVS.

Although posttranscriptional regulation of RNA has been extensively studied in the context of immune responses, the known functions of RNA in immune signaling complexes are limited (67). Therefore, the concept that RNA could modulate the activation of higher-order protein complexes, which are a feature of innate immune signaling (68), may broadly apply to other immune signaling adaptors.

Materials and methods

Cell culture

Human embryonic kidney 293T (referred to as 293T throughout this manuscript) and NIH3T3 cells were grown in Dulbecco's modified Eagle's medium (DMEM; Thermo Fisher) supplemented with 10% fetal bovine serum (HyClone), 25 mM HEPES (Thermo Fisher), 1X nonessential amino acids (Thermo Fisher), and 1X PSG (Thermo Fisher). Cells were continuously verified as mycoplasma free using the LookOut Mycoplasma PCR detection kit (Sigma-Aldrich). Primary human macrophages were derived from CD14+ monocytes (Bloodworks) in RPMI 1640 medium supplemented with 10% fetal bovine serum, 1X PSG, and 50 ng/mL M-CSF (Shenandoah).

Virus models

Sendai virus Cantrell strain (SenV; Charles River) and green fluorescent protein (GFP)-encoding VSV (GFP-VSV), gifts of the Gale lab, were amplified in chicken eggs and BHK-21 cells, respectively (69). Encephalomyocarditis virus (EMCV; ATCC) was grown and titered in Vero cells (70).

Plasmids and cloning

MAVS and RLR pathway constructs

pEFTak empty vector and FLAG-MAVS and pEFBos FLAG-N-RIG and FLAG-N-MDA5 have been described before (60). pEFTak FLAG-MAVS ΔCARD, FLAG-MAVS ΔTM, FLAG-MAVS ΔCARD+ΔTM and FLAG-MAVS Δ103-467 were generated by PCR mutagenesis of pEFTak FLAG-MAVS with linkers on primers for in-frame cloning. pEFTak FLAG-murineMAVS was cloned using InFusion cloning (Takara) of a PCR fragment of the MAVS open reading frame amplified from NIH3T3 cell complementary DNA (cDNA) into *NotI*- and *PmeI*-digested pEFTak FLAG vector. pEFTak FLAG-MAVS 103-467, Δ1-102, Met¹⁴², Met³⁰³, Met³⁶⁷, and Met⁴⁴⁹ were constructed by InFusion cloning of PCR fragments amplified from pEFTak FLAG-MAVS into *NotI*- and *PmeI*-digested pEFTak FLAG vector.

APOBEC1 constructs

pEFTak APOBEC1 was generated using InFusion cloning of the murine APOBEC1 open reading frame (gift of Dr. Jennifer Hyde) amplified by PCR, annealed primers coding for a 15 amino acid linker (protein sequence: SGSETPGTSE-SATPE), and *NotI*- and *PmeI*-digested pEFTak FLAG vector. Similarly, *NotI*- and *PmeI*-digested pEFTak FLAG vector, annealed primers for the linker, and PCR fragments of the entire MAVS coding sequence or the terminal 40 amino acids of MAVS were recombined using InFusion cloning to generate pEFTak APOBEC1-MAVS^{FL} and APOBEC1-MAVS^{C-term} respectively.

3xFV-N-RIG

pRRL 3xFV-N-RIG lentiviral vector was constructed by using InFusion cloning of a synthe-

sized gene fragment (IDT) containing the N-terminal CARDs of murine RIG-I (amino acids 1-229) downstream of 3 tandem copies of FKBPI2 carrying the F36V mutation (called "FV" domains) into *BamHI*-cut pRRL-Blast vector. Two of the three copies contained silent mutations to prevent DNA recombination.

GLuc reporter constructs

pTRIP *IFNB1*^{2X}-GLuc reporter lentiviral vector was constructed by InFusion cloning of PCR amplified *IFNB1* promoter enhaceosome elements [-110 to -37 upstream of the transcription start site (Twist gene fragment)], ligated together with *BamHI*, into *SmaI*-cut pTRIP ISRE-GFP (71) (Gift of N. Heaton). Further, the GFP gene was replaced with codon-optimized *Gaussia* luciferase open reading frame fused to the mODC-PEST domain (Twist gene fragment) by InFusion cloning into *XhoI*- and *XbaI*-cut vector. pTRIP PRDII4X-GLuc reporter lentiviral vector was constructed by InFusion cloning of PCR-amplified Twist gene fragment into *SmaI*- and *XbaI*-cut pTRIP *IFNB1*^{2X}-GLuc. All primer and gene fragment sequences and a list of plasmids are provided in data S3.

Generation of 293T RIG-I^{KO}, 293T RIG-I+MDA5^{DKO}, 293T MAVS^{KO}, and 293T IRF3^{KO} cells

293T cells deleted for RLR pathway proteins were generated by CRISPR-Cas9-mediated gene editing. RIG-I^{KO}: Two guides targeting just upstream of the transcription start site (GCTAGTGAGGCACAGCCTGCGGG) and in exon 1 (CCCAGGTTGTGGTAAGATCTCC), respectively. MAVS^{KO}: Single guide targeting exon 5 (CCTCAGCCCTGACCTCCAGCG). IRF3^{KO}: Single guide targeting exon 2 (CCAC-TGGTGCAATGTTCCC) (72, 73). 293T cells were transfected with the respective guide containing plasmids (pX330-sgRIGI-1 and pX330-sgRIGI-2, pX330-sgMAVS, or pX330-sgIRF3) along with pcDNA-Blast (encoding blasticidin resistance). Individual clones were selected following 0.2 µg/mL blasticidin selection and then screened for RIG-I, MAVS, or IRF3 protein expression by immunoblot. Clones with loss of protein expression and signaling function were further validated by sequencing of amplicons spanning targeted regions. 293T RIG-I+MDA5^{DKO} cells were generated by transducing 293T RIG-I^{KO} cells with lentivirus (packaged from pRRL-puro gIFIH1) encoding Cas9 and guide RNA against exon 1 (CGTCTT-GGATAAGTGCATGG). Individual clones were selected with 1 µg/mL puromycin and screened for loss of MDA5 protein expression and signaling function.

Generation and stimulation of 293T

3xFV-N-RIG cells

Lentivirus for 3xFV-N-RIG expression was produced in 293T cells by cotransfection of pRRL 3xFV-N-RIG, pMD2.G, and psPAX2. Stable

293T^{WT} and 293T IRF3^{KO} cell lines transduced with this lentivirus were selected using 0.5 µg/mL blasticidin. Stable 293T RIG+MAVS^{DKO} transduced with this virus were selected FACS sorting on co-expressed mCherry. Cell lines were maintained in cDMEM supplemented with 0.2 µg/mL blasticidin. RLR signaling was activated by treatment with 10 nM B/B homodimerizer (AP20187; Clonetech) for the indicated amount of time.

Generation of 293T *IFNB1*^{2X}-GLuc and PRDII^{4X}-GLuc cells

Lentivirus for *IFNB1*^{2X}-GLuc or PRDII^{4X}-GLuc was produced in 293T cells by cotransfection of pTRIPZ *IFNB1*^{2X}-GLuc or PRDII^{4X}-GLuc with pMD2.G, and psPAX2 and was used to transduce 293T cells. Single transduced cells were cloned by dilution and colony outgrowth, and clones were screened for their ability to produce GLuc in the supernatant using the *Gaussia* Glow kit (Thermo Fisher).

RT-qPCR

RNA was extracted using TRIzol (Thermo Fisher) or RNA columns (Machery-Nagel), and cDNA was generated using the PrimeScript RT-PCR kit (Takara). RT-qPCR was performed using a ViiA7 Real Time PCR instrument (Applied Biosciences) with TaqMan Universal PCR master mix II - UNG (Thermo Fisher). Primers for RT-qPCR are described in data S3.

Immunoblotting

For sucrose gradient ultracentrifugation, immunoprecipitation, and MAVS activity assays, protein samples in assay-specific buffers were prepared with 1X to 2X final concentration of Laemmli buffer (Bio-Rad) with 2.5% β-ME and immunoblotted as described below. Whole cell lysates were prepared in a modified RIPA buffer (10 mM Tris pH 7.4, 150 mM NaCl, 0.5% sodium deoxycholate, and 1% Triton X-100) supplemented with protease-phosphatase inhibitor cocktail (Sigma-Aldrich) and clarified by centrifugation at 7500g for 10 min at 4°C. Protein concentration was determined by Bradford assay (Bio-Rad). Equal amounts of protein sample in 1X Laemmli buffer with 2.5% β-ME were boiled and resolved by SDS-PAGE (Tris-Glycine gels; Bio-Rad) and transferred to methanol-activated PVDF membranes (Bio-Rad) by wet transfer. For probing of hard-to-detect targets, transferred membranes were fixed in membrane fixation buffer (7% acetic acid, 3% glycerol, 40% ethanol in water) prior to blocking with 3% BSA in tris-buffered saline with 0.1% Tween (TBS-T). Transferred membranes were incubated with relevant primary antibodies in 3% BSA in TBS-T with shaking for 1 to 2 hours at room temperature or overnight at 4°C. After washing three times with TBS-T, membranes were incubated with species-specific horseradish peroxidase-conjugated secondary

antibodies. Chemiluminescence was detected using a Bio-Rad ChemiDoc XRS+ imaging instrument. Gels were quantified by densitometry using FIJI (74). All antibodies are described in data S3.

Subcellular fractionation for crude mitochondrial extracts

For subcellular fractionation of crude mitochondrial extracts, 293T cells were harvested by pipetting in PBS, resuspended in 500 μ L cold hypotonic buffer (10 mM Tris pH 7.4, 10 mM KCl, 1.5 mM MgCl₂, 0.5 mM EGTA, and 1X protease-phosphatase inhibitor) for 15 min on ice, and were then disrupted by 70 strokes of a tight pestle in 1 mL Dounce homogenizers (Omni). Alternatively, cells were collected in cold PBS supplemented with 1X protease-phosphatase inhibitor for 15 min on ice and were then disrupted by passing through a 27^{1/2}-gauge syringe needle 10 times. These mechanically disrupted lysates were centrifuged at 1000g for 5 min at 4°C to pellet nuclei and cell debris. Supernatants were then transferred to new tubes and centrifuged at 10,000g for 10 min at 4°C. Supernatants (cytosolic fraction; “cyto”) were transferred to new tubes or discarded. Pellets (crude mitochondrial fraction; “mito”) were resuspended in assay-specific buffers (see below). Protein concentration in cytosolic and crude mitochondrial fractions was measured by Bradford Assay.

MAVS activity assay for *in vitro* phosphorylation of IRF3 and p65

MAVS activity assay was adapted from Zeng *et al.*, using IRF3^{KO} cells to ensure that 293T^{WT} cytoplasmic lysates are the only source of IRF3 in the system in place of ³⁵S-labeled IRF3 (32). The MAVS signalosome was activated in 293T IRF3^{KO} or 293T 3xFV-N-RIG IRF3^{KO} cells cultured in 10 cm plates by SenV infection [100 HAU/mL (HAU, hemagglutinin units), 16 hours post-infection (hpi)] and B/B treatment [10 nM, 3 hours posttreatment (hpt)], respectively. 293T^{WT} cells were concurrently cultured in a 10 cm plate and were left unstimulated. 5% of cells were stored for immunoblotting of whole cell lysates. Cells were fractionated as described above to generate cytosolic extract (“Cyto”) from 293T^{WT} cells and crude mitochondrial pellets from IRF3^{KO} cells. Mitochondrial pellets (“Mito”) were washed once with 200 μ L mitochondrial reconstitution buffer (MRB; 20 mM HEPES-KOH pH 7.5, 10% glycerol, 0.5 mM EGTA), and resuspended in 50 μ L MRB with 1% DDM and 1X protease-phosphatase inhibitor. After incubation on ice for 10 min, mitochondrial and cytosolic lysates were centrifuged at 5000g at 4°C for 5 min to pellet debris. 10 μ g of mitochondrial lysate was mixed with RNaseIN as control, or with RNase, and were incubated for 15 min on ice. 40 μ g of cytosolic extract from 293T^{WT} cells was added to each sample in

a final volume of 30 μ L. 10 μ L of 4X MAVS activity buffer [80 mM HEPES-KOH pH 7.0, 10 mM adenosine triphosphate (ATP), 20 mM MgCl₂] was then added for a final reaction volume of 40 μ L, and samples were incubated for 1 hour at 30°C with gentle shaking (250 rpm) in a Thermomixer. Reactions were stopped by the addition of Laemmli buffer and boiling prior to SDS-PAGE. The MAVS signalosome was activated in 293T R+M^{DKO} cells and 293T R+M^{DKO} 3xFV-N-RIG cells by FLAG-MAVS transfection (10 ug, 48 hpt) and B/B-treatment (10 nM, 12 hpt) respectively and subjected to a similar protocol as above. A similar protocol was used for analysis of *in vitro* IRF3 phosphorylation by fractionated mitochondrial extracts from SenV-infected cells: 10 μ L each fraction (2% of each 500 μ L fraction from 5 mL sucrose columns) was incubated with unstimulated 293T^{WT} cytosolic extract in MAVS activity buffer. For *in vitro* phosphorylation of NF- κ B p65, 293T^{WT} cells were infected with SenV (250 HAU/mL, 16 hpi). 10 μ g of mitochondrial lysates from these cells were treated with RNase or RNaseIN and incubated with 40 μ g unstimulated cytosolic extract from 293T^{WT} cells and 4X activity buffer (80 mM Tris-HCL pH 7.5, 10 mM ATP, 20 mM MgCl₂) in a final reaction volume of 40 μ L. Following SDS-PAGE, transfer to PVDF membranes, and membrane fixation, samples were immunoblotted for IRF3 p-S386, IRF3, RELA/p65 p-536, RELA/p65, or MAVS.

RNase-dependent shift assays by sucrose gradient ultracentrifugation

Sucrose gradient ultracentrifugation to identify RNase-dependent shift was performed as described by Caudron-Herger *et al.* with modifications (37). Sucrose gradients in 5 mL or 14 mL ultracentrifuge tubes (Beckman-Coulter) were prepared by sequential addition of 5 to 50% sucrose in 5% steps in gradient buffer (10 mM Tris pH 7.4, 100 mM NaCl, 1 mM EDTA), with freezing between the addition of each fraction (1.2 mL per fraction). Cytosolic and crude mitochondrial fractions from 293T, 293T RIG-I^{KO}, 293T R+M^{DKO}, or NIH3T3 cells in 10 cm plates with the indicated treatments [SenV infection: 100 HAU/mL, 14 to 16 hpi; EMCV infection: multiplicity of infection (MOI) 0.01, 16 hpi; transfected with pEFTak FLAG-MAVS or pEFTak FLAG-murineMAVS or pEFBos FLAG-N-RIG or pEFBos FLAG-N-MDA5, 10 μ g, 24 hpt using TransIT X2 (Mirus) transfection reagent] were isolated as described above. Mitochondrial pellets were lysed in PBS with 1% n-dodecyl- β -D-maltoside (DDM; Sigma-Aldrich) and 1X protease-phosphatase inhibitor, and 10% cytosolic extracts were added back to mitochondrial lysates. Following protein quantification, equal amounts (~500 μ g) of each sample were treated with RNaseIN as control (Promega, 40 U), or an RNase cocktail

[per sample: RNase A (Thermo Fisher, 1 μ g), RNase I (Thermo Fisher, 5 U), RNase T1 (Thermo Fisher, 500 U) and RNase III (Thermo Fisher, 1 U)] for 1 hour on ice. Treated samples were loaded on 5 to 50% sucrose gradient columns and ultracentrifuged using an SW40Ti rotor at 40,000g for 18 hours at 4°C. Following ultracentrifugation, equal fractions (1.25 mL) were transferred into new tubes by careful pipetting from the top of each tube. For samples fractionated in 14 mL columns, protein in each fraction was precipitated by mixing 0.7 mL of each fraction with 1.5 mL of 100% ethanol and 0.5 μ L GlycoBlue (Thermo Fisher) at -20°C overnight. Precipitated protein was pelleted by centrifugation at 13,000g for 30 min at 4°C, washed once with 70% ethanol, and dried. Protein pellets were resuspended in 1X Laemmli buffer with β -ME and dissolved by boiling at 95°C for 10 min with shaking in a Thermomixer. Equal volume of each sample was resolved by SDS-PAGE and immunoblotted with the relevant antibodies.

irCLIP to detect crosslinked RNA-protein complexes

To test the RNA-binding ability of MAVS and MAVS constructs, irCLIP was performed as described by Zarnegar *et al.* with slight modifications (40). For endogenous MAVS irCLIP, primary human macrophages derived from CD14⁺ monocytes, 293T^{WT} or 293T R+M^{DKO} cells were cultured in 6-well plates and infected with SenV (100 HAU/mL, 16 hpi) or not as indicated. For FLAG-tagged MAVS constructs, 293T MAVS^{KO} or NIH3T3 cells cultured in 6-well plates were transfected with the indicated FLAG-tagged plasmids for 16 hours. For irCLIP of overexpressed MAVS constructs, mitochondrial extracts were prepared from 293T MAVS^{KO} cells as described above, unless experiment involved any MAVS constructs lacking the transmembrane domain (FLAG-MAVS 103-467, Δ TM, Δ CARD+ Δ TM), in which case, whole cell lysates were used. At time of harvest, cells were washed with PBS, cross-linked with 254 nm UV-C light (0.15 J/cm²), and lysed in 200 μ L irCLIP lysis buffer (50 mM Tris pH 7.5, 150 mM NaCl, 1 mM EDTA, 1% Triton X-100, 0.1% SDS, 1X protease inhibitor). After sonication in ice slurry, lysates were clarified by centrifugation at 5000g for 10 min at 4°C, quantified by Bradford assay, and concentrations were equalized. 5% of each sample was stored for input control. 200 μ g of each lysate was incubated with 20 μ L Protein G Dynabeads (Thermo Fisher) pre-conjugated with 4 μ g mouse anti-FLAG M2 antibody (Sigma-Aldrich) or rabbit anti-MAVS (Bethyl) in a final volume of 500 μ L irCLIP lysis buffer for 2 hours at 4°C with rotation. Beads were then sequentially washed with the following ice-cold buffers: twice with 1 mL irCLIP lysis buffer, twice with 1 mL high stringency buffer (20 mM

Tris pH 7.5, 120 mM NaCl, 25 mM KCl, 5 mM EDTA, 1% Triton X-100, 1% sodium deoxycholate, 0.1% SDS), twice with 1 mL high salt buffer (20 mM Tris pH 7.5, 500 mM NaCl, 5 mM EDTA, 1% Triton X-100, 1% NaDOC), twice with 1 mL low salt buffer (20 mM Tris pH 7.5, 5 mM NaCl, 5 mM EDTA, 1% Triton X-100), and twice with 1 mL NT2 buffer (50 mM Tris pH 7.5, 150 mM NaCl, 1 mM MgCl₂, 0.05% NP-40). 10% beads were then removed for immunoblot analysis, and the rest of the beads were then resuspended in 30 μL NT2 buffer containing 25 ng/mL RNase A and 15% PEG400 (Sigma-Aldrich) for on-bead RNase digestion at 30°C for 15 min with shaking (1200 rpm) in a Thermomixer. RNase digestion was quenched by the addition of 1 mL high stringency buffer. Beads were washed twice with 0.3 mL PNK wash buffer (50 mM Tris pH 7.0, 10 mM MgCl₂), and then resuspended in 30 μL PNK dephosphorylation mix [1X PNK buffer (Promega), 0.5 μL RNaseIN, 1 μL T4 PNK (Promega), 4 μL PEG400]. Dephosphorylation reactions were conducted at 37°C for 60 min with shaking (1200 rpm) in a Thermomixer. Dephosphorylation mix was removed, and beads were washed with 0.3 mL PNK wash buffer. For ligation of IRDye-800-conjugated oligo to RNA crosslinked to protein, beads were resuspended in 30 μL RNA ligation mix [1X RNA ligase I buffer (NEB), 1 μL RNA ligase I (NEB), 0.5 μL IRDye800-labeled oligonucleotide (40), 5 μL PEG400, and 0.5 μL RNaseIN] and incubated for 16 hours at 16°C with shaking in Thermomixer (1200 rpm). Ligation mix was then removed, and beads were washed twice with 0.3 mL PNK wash buffer, prior to elution of RNA-protein complexes in 20 μL 1X LDS Buffer (Thermo Fisher) + 10% β-ME at 80°C for 10 min. 5 μL of eluates, as well as input controls, were then resolved by SDS-PAGE on 4-12% Bis-Tris NuPAGE gels (Thermo Fisher) and transferred to nitrocellulose membranes. Fluorescent RNA-protein complexes in the eluates were visualized on a LiCOR Odyssey FC imager. The same membranes were then subjected to immunoblotting using HRP-conjugated anti-FLAG M2 or anti-MAVS antibody.

Prediction of disorder conservation in MAVS

Prediction of intrinsic disorder in human MAVS was conducted using IUPred3 (43) and FuzPred (75) web portals. The IUPred3 package was used for the analysis of disorder conservation in MAVS homologs downloaded from NCBI and Ensembl.

Identification of MAVS-associated RNAs using APOBEC1-mediated profiling

293T cells seeded in 12-well plates were transfected with 0.5 μg plasmid encoding APOBEC1, APOBEC1-MAVS^{C-term}, and APOBEC1-MAVS^{FL} using the TransIT X2 transfection reagent in bi-

ological triplicate. At 24 hours post-transfection, RNA was extracted using TRIzol, treated with Turbo DNase I (Thermo Fisher), cleaned by phenol-chloroform extraction, and precipitated. Total RNA stranded library preparation with rRNA depletion and paired end 100 bp sequencing using the DNBseq platform was performed through BGI Genomics.

RNA-sequencing data was subjected to quality control and adaptor trimming using SOAPnuke (76). Additional quality control was performed using fastqc and multiqc (77, 78); all samples passed thresholding and were retained. A snakemake pipeline using samtools, Rsamtools, bedtools, and pybedtools was used to orchestrate analysis (https://github.com/ksom/seq_pipeline) (79–83). Reads were aligned to GRCh38 using STAR (84). The Bullseye pipeline (<https://github.com/mflamand/Bullseye>) was used to detect C-to-T editing at sites with at least 10 reads of coverage per sample, with an edit ratio between 2 and 95% (minEdit=5) and an edit ratio at least 1.5-fold-higher than control samples (editFoldThreshold=1.5) (52, 53).

Validation of PMAIP1 editing by Sanger sequencing

293T cells were transfected with 0.5 μg plasmids encoding APOBEC1-MAVS^{C-term} and APOBEC1-MAVS^{FL} for 24 hours using Mirus X2. After RNA extraction and cDNA preparation using the PrimeScript RT kit, the *PMAIP1* 3'UTR was amplified by PCR (primers, data S3), and purified amplicons were subjected to Sanger sequencing. The MultiEditR web tool was used to analyze C-to-T editing in .ab1 chromatograms at sites called by Bullseye (85).

CLIP-RT-qPCR

293T cells seeded in six-well plates were transfected with plasmids encoding FLAG-MAVS or FLAG-MAVS Δ103-467 using TransIT X2. For experiments comparing FLAG-MAVS Δ103-467 and FLAG-MAVS Δ1-102, cells were treated with 100 U/mL IFN-β (PBL Assay Science) at 16 hpt for 24 hours. At 24 hpt, cells were washed with PBS, crosslinked with 254 nm UV-C light (0.15 J/cm²), and lysed in 200 μL irCLIP lysis buffer supplemented with protease-phosphatase and RNase inhibitors. After sonication in ice slurry, lysates were clarified by centrifugation at 5000g for 10 min at 4°C, quantified by Bradford assay, and concentrations were equalized. After removing 20 μg lysate for input RNA (10%), 200 μg lysates were incubated with washed Protein G Dynabeads bound to anti-FLAG antibody (25 μL beads and 4 μg antibody per sample) in irCLIP lysis buffer for 2 hours at 4°C with rotation. Beads were then washed twice with 1 mL irCLIP lysis buffer, twice with 1 mL high stringency buffer, and twice with PBS. Beads were resuspended in 100 μL PBS, and 10% beads were removed for immunoblot analysis. After the addition of 10 μL 10X Turbo DNase

buffer and 2 μL Turbo DNase I, beads were incubated at 37°C with shaking (1000 rpm) in a Thermomixer. RNA was then eluted from beads by incubation with 5 μg Proteinase K (Thermo Fisher) at 50°C with shaking (1000 rpm). After removal of supernatant, beads were washed twice with 100 μL PBS and washes were pooled with the eluates. RNA was purified from input and IP samples using TRIzol LS (Thermo Fisher). Equal volumes of eluted RNA were used for cDNA synthesis, quantified by RT-qPCR, and normalized to RNA levels in input samples. CLIP-RT-qPCR of RNA bound to endogenous MAVS was performed similarly from uninfected and SenV-infected (100 HAU/mL, 20 hours) 293T cells, except that lysates were incubated with Protein G Dynabeads bound to rabbit anti-MAVS or normal rabbit immunoglobulin G (IgG). Fold enrichment was calculated with the enrichment over input in FLAG-MAVS Δ103-467 for each IgG set as 1.

Immunofluorescence microscopy

293T cells seeded in eight-well chamber slides (Millipore) were transfected with the indicated FLAG-tagged APOBEC1-MAVS or control constructs. At 24 hours after transfection, cells were washed with PBS and fixed with 4% paraformaldehyde for 10 min. Cells were permeabilized with 0.2% Triton X-100 in blocking buffer (3% BSA in PBS). Permeabilized cells were incubated with primary anti-FLAG antibody (1:2500) for 1 hour, washed with PBS, and were then incubated in AlexaFluor conjugated secondary antibody (1:2500; Thermo Fisher) and DAPI (1:1000) for 1 hour. After further PBS washes, chamber slides were mounted using ProLong Gold (Thermo Fisher). Images were acquired using a Nikon C2 confocal microscope.

SDD-AGE for MAVS oligomerization

Crude mitochondrial pellets were generated from SenV-infected (200 HAU/mL, 12 hpi), FLAG-MAVS-transfected (10 μg, 16 hpi, TransIT X2 transfection reagent), or unstimulated 293T cells as described above. Mitochondrial pellets were resuspended in 50 μL PBS, divided equally into three separate tubes, and treated with RNaseIN, RNase cocktail, or 30 μM β-ME. Following incubation on ice for 30 min, an equal volume of 2X SDD-AGE sample buffer [2% SDS, 10% glycerol, 0.02% bromophenol blue in 0.5X tris-borate-EDTA (TBE)] was added to each tube. 10% of sample was stored for input controls, supplemented with Laemmli buffer, boiled, and immunoblotted by SDS-PAGE. 50% of the sample was loaded on a 1.5% agarose gel prepared in 1X TBE buffer. Samples were resolved by vertical electrophoresis (70V, 120 mA, 1 hour) in SDD-AGE running buffer (1X TBE, 0.1% SDS), and transferred (20V, 250 mA, constant voltage, overnight at 4°C) to PVDF membranes in SDD-AGE transfer buffer [25 mM Tris (pH 8.3), 192 mM glycine, 20% (v/v) ethanol].

Transferred membranes were fixed with 0.25% glutaraldehyde in PBS for 20 min with shaking and immunoblotted with anti-FLAG or anti-MAVS primary antibodies.

Immunoprecipitation and mass spectrometry

293T cells were seeded in two 10 cm plates per condition and transfected with pEFTak FLAG-MAVS or empty vector using the Mirus Transit X2 transfection reagent. Cells were harvested at 20 hours after transfection and crude mitochondrial extracts were prepared by mechanical disruption using a 27^{1/2} gauge needle as described above. Crude mitochondrial pellets were lysed in 300 μL IP-MS lysis buffer (25 mM Tris pH 7.5, 150 mM NaCl, 5 mM MgCl₂, 0.5% DDM) supplemented with protease-phosphatase inhibitor and RNase inhibitor. 0.5 mg of mitochondrial lysates were incubated with washed Protein G Dynabeads prebound to anti-FLAG antibody (35 μL beads with 8 μg antibody per sample) in IP-MS wash buffer (25 mM Tris pH 7.5, 150 mM NaCl, 5 mM MgCl₂, 0.1% DDM) in a final volume of 1 mL for 4 hours at 4°C with rotation. Beads were then washed twice with 1 mL IP-MS wash buffer. MAVS + RNase samples were then incubated with 0.5 mL IP-MS wash buffer containing RNase A (1 μg/mL) and RNase T1 (1 U/μL) for 30 min at room temperature with rotation. Concurrently, empty vector and MAVS-RNase samples were incubated in 0.5 mL IP-MS wash buffer containing RNase inhibitor. Beads were then washed twice with 1 mL IP-MS wash buffer, and twice in wash buffer without DDM. After moving beads to fresh tubes, samples were subjected to on-bead reduction, alkylation, and tryptic digest. Bound proteins were reduced with 5 mM DTT (Sigma-Aldrich) in 50 mM TEAB (Thermo Fisher) in a final volume of 100 μL for 30 min at room temperature, followed by alkylation with 10 mM iodoacetamide (Thermo Fisher) for 30 min at room temperature in the dark. Proteins were digested with 1 μg MS-grade trypsin (Thermo Fisher) at 37°C overnight with gentle shaking (800 rpm) in a Thermomixer. After addition of another 1 μg trypsin, samples were similarly incubated for 4 hours. After collecting post-trypsin supernatants, beads were washed twice with 50 μL of 50 mM TEAB and washes were pooled with digested peptides.

Digested peptide samples were acidified with trifluoroacetic acid (TFA) to a final concentration of 0.5% and then desalted using C18 StageTips according to the published protocol with minor adjustments (86). StageTips were activated with 50 μL methanol, followed by sequential addition of 50 μL StageTip buffer B [80% acetonitrile (ACN) in 0.1% TFA] and 50 μL StageTip buffer A (0.1% TFA, 5% ACN). After sample loading, peptides were washed with 50 μL StageTip buffer A. Peptides from StageTips were eluted using 50 μL 45% ACN, 0.1% TFA into a 96-well plate. Samples were then dried

down by vacuum centrifugation and resuspended in StageTip buffer A. Peptides were separated on an EASY-nLC 1200 System (Thermo Fisher) using 20 cm long fused silica capillary columns (100 μm ID, laser-pulled in-house using the Sutter P-2000) packed with 3 μm 120 Å reversed phase C18 beads (Dr. Maisch). The liquid chromatography (LC) gradient was 90 min long with 5 to 35% B at 300 nL/min. LC solvent A was 0.5% acetic acid and LC solvent B was 0.5% acetic acid, 80% ACN. MS data was collected with a Thermo Fisher Orbitrap Fusion Lumos using a data-independent acquisition (DIA) method with a 120K resolution Orbitrap MS1 scan and 12 m/z isolation window, and 30K resolution Orbitrap MS2 scans for precursors from 400 to 1000 m/z.

Data .raw files were converted to .mzML using MSConvert (v3.0.21251-d2724a5) and spectral libraries were built using MSFragger-DIA with FragPipe (v20.0) (87) with quantification through DIA-NN v1.8.2 (88). Database search was against the UniProt human database (updated 6 July 2023) with supplemental spike-in of common contaminants, containing 20477 sequences and 20477 reverse-sequence decoys. For the MSFragger analysis, both precursor and initial fragment mass tolerances were set to 20 ppm and spectrum deisotoping, mass calibration, and parameter optimization were enabled. Enzyme specificity was set to "stricttrypsin" and up to two missed trypsin cleavages were allowed. Methionine oxidation, N-terminal acetylation, serine, threonine, and tyrosine phosphorylation, -18.0106 Da on N-terminal glutamic acid, and -17.0265 Da on N-terminal glutamine and cysteine were set as variable modifications. Cysteine carbamidomethylation was set as a fixed modification. The maximum number of variable modifications per peptide was set to 3. FragPipe/DIA-NN output files were processed and analyzed using the Perseus software package v2.0.7.0 (89). Rows were retained only if at least one of the three experimental groups had at least three of five valid values. Data imputation was performed using a modeled distribution of MS intensity values downshifted by 1.8 and having a width of 0.2. Expression values (protein MS intensities) were log₂-transformed and normalized by subtracting the median log₂ expression value from each expression value within each MS run. For statistical testing of significant differences in enrichment, a two-sample Student's t test was applied.

Enriched proteins were filtered for common contaminants of IP-MS experiments using the CRAPome database, and only proteins found in <30% of CRAPome datasets were chosen for further analysis (90). Interactome network analysis was performed and visualized using the STRING app in Cytoscape (91, 92). Gene set enrichment analysis of MAVS-interacting proteins was performed on a pre-ranked list of identified proteins, with log₂FC(MAVS_CTRL-EV) x -log₁₀

(P value) as the ranking metric (57, 58). Network analysis of enriched GO: Biological Process pathways was performed and visualized with Enrichment Map and Cytoscape (92, 93).

Targeted siRNA screening

293T *IFNB1*^{2X}-GLuc or 293T PRDII^{4X}-GLuc cells plated in 96-well plates (50,000 cells/well) in media without antibiotics were transfected with 1 pmol/well siRNA (Silencer Select, Thermo Fisher) using Lipofectamine RNAiMAX (Thermo Fisher) in technical triplicate. At 36 hours post-siRNA transfection, media was exchanged, and cells were transfected with 50 ng/well of in vitro transcribed poly-U/UC RNA using the TransIT X2 reagent (60). At 24 hours post-poly-U/UC RNA transfection, 10 μL supernatant from each well was transferred to white opaque 96-well plates, wherein it was mixed with *Gaussia* Glow assay buffer with 1X coelenterazine (Thermo Fisher), and luminescence was read on a Biotek Synergy plate reader. Cellular viability was measured using Cell Titer-Glo (Promega). Secondary screen for *IFNB1* mRNA induction was performed similarly in 293T cells seeded in 48-well plates. RNA was extracted at 24 hours post-poly-U/UC RNA transfection using TRIzol and RT-qPCR was performed as described. All siRNA sequences, assay IDs, and RT-qPCR primers are listed in Data File S3.

Viral restriction assay

293T cells plated in 24-well plates (150,000 cells/well) in media without antibiotics were transfected with 2.5 pmol/well siRNA using Lipofectamine RNAiMAX. At 36 hours after siRNA transfection, media was exchanged, and cells were transfected with 50 ng/well poly-U/UC RNA. At 16 hours after poly-U/UC transfection, cells were infected with VSV-GFP at an MOI of 0.001 in low-serum media for 1 hour with shaking. Supernatants were harvested at 24 hpi and serial dilutions were subjected to plaque forming assays on Vero cell monolayers prior to fixation with 4% paraformaldehyde and staining with crystal violet as described previously (70).

Statistics

Unless otherwise noted, at least three independent biological replicates were performed for all experiments. Dots represent the mean value of technical replicates from an individual biological replicate performed in the indicated cell lines and conditions. Summary graphs and error bars represent means ± SEM. Ordinary one-way or two-way analysis of variance (ANOVA) with Tukey's multiple comparison test and unpaired t test were used for comparisons and were performed using GraphPad Prism. All comparisons and tests are noted in the figure legend in which they appear.

REFERENCES AND NOTES

- J. Rehwinkel, M. U. Gack, RIG-I-like receptors: Their regulation and roles in RNA sensing. *Nat. Rev. Immunol.* 20,

- 537–551 (2020). doi: [10.1038/s41577-020-0288-3](https://doi.org/10.1038/s41577-020-0288-3); pmid: [3220325](https://pubmed.ncbi.nlm.nih.gov/3220325/)
2. R. Savan, M. Gale Jr., Innate immunity and interferon in SARS-CoV-2 infection outcome. *Immunity* **56**, 1443–1450 (2023). doi: [10.1016/j.immuni.2023.06.018](https://doi.org/10.1016/j.immuni.2023.06.018); pmid: [37437537](https://pubmed.ncbi.nlm.nih.gov/37437537/)
 3. Y. J. Crow, J.-L. Casanova, Human life within a narrow range: The lethal ups and downs of type I interferons. *Sci. Immunol.* **9**, eadm8185 (2024). doi: [10.1126/sciimmunol.adm8185](https://doi.org/10.1126/sciimmunol.adm8185); pmid: [38968338](https://pubmed.ncbi.nlm.nih.gov/38968338/)
 4. H. Kato et al., Differential roles of MDA5 and RIG-I helicases in the recognition of RNA viruses. *Nature* **441**, 101–105 (2006). doi: [10.1038/nature04734](https://doi.org/10.1038/nature04734); pmid: [16625202](https://pubmed.ncbi.nlm.nih.gov/16625202/)
 5. S. M. Horner, H. M. Liu, H. S. Park, J. Briley, M. Gale Jr., Mitochondrial-associated endoplasmic reticulum membranes (MAM) form innate immune synapses and are targeted by hepatitis C virus. *Proc. Natl. Acad. Sci. U.S.A.* **108**, 14590–14595 (2011). doi: [10.1073/pnas.1110133108](https://doi.org/10.1073/pnas.1110133108); pmid: [21844353](https://pubmed.ncbi.nlm.nih.gov/21844353/)
 6. E. Dixit et al., Peroxisomes are signaling platforms for antiviral innate immunity. *Cell* **141**, 668–681 (2010). doi: [10.1016/j.cell.2010.04.018](https://doi.org/10.1016/j.cell.2010.04.018); pmid: [20451243](https://pubmed.ncbi.nlm.nih.gov/20451243/)
 7. F. Hou et al., MAVS forms functional prion-like aggregates to activate and propagate antiviral innate immune response. *Cell* **146**, 448–461 (2011). doi: [10.1016/j.cell.2011.06.041](https://doi.org/10.1016/j.cell.2011.06.041); pmid: [21782231](https://pubmed.ncbi.nlm.nih.gov/21782231/)
 8. R. Fang et al., MAVS activates TBK1 and IKK ϵ through TRAFs in NEMO dependent and independent manner. *PLoS Pathog.* **13**, e1006720 (2017). doi: [10.1371/journal.ppat.1006720](https://doi.org/10.1371/journal.ppat.1006720); pmid: [29125880](https://pubmed.ncbi.nlm.nih.gov/29125880/)
 9. S. Liu et al., Phosphorylation of innate immune adaptor proteins MAVS, STING, and TRIF induces IRF3 activation. *Science* **347**, aaa2630 (2015). doi: [10.1126/science.aaa2630](https://doi.org/10.1126/science.aaa2630); pmid: [25636800](https://pubmed.ncbi.nlm.nih.gov/25636800/)
 10. S. Liu et al., MAVS recruits multiple ubiquitin E3 ligases to activate antiviral signaling cascades. *eLife* **2**, e00785 (2013). doi: [10.7554/elife.00785](https://doi.org/10.7554/elife.00785); pmid: [23951545](https://pubmed.ncbi.nlm.nih.gov/23951545/)
 11. E. Meylan et al., Cardif is an adaptor protein in the RIG-I antiviral pathway and is targeted by hepatitis C virus. *Nature* **437**, 1167–1172 (2005). doi: [10.1038/nature04193](https://doi.org/10.1038/nature04193); pmid: [16177806](https://pubmed.ncbi.nlm.nih.gov/16177806/)
 12. R. B. Seth, L. Sun, C.-K. Ea, Z. J. Chen, Identification and characterization of MAVS, a mitochondrial antiviral signaling protein that activates NF- κ B and IRF3. *Cell* **122**, 669–682 (2005). doi: [10.1016/j.cell.2005.08.012](https://doi.org/10.1016/j.cell.2005.08.012); pmid: [16125763](https://pubmed.ncbi.nlm.nih.gov/16125763/)
 13. L.-G. Xu et al., VISA is an adapter protein required for virus-triggered IFN- β signaling. *Mol. Cell* **19**, 727–740 (2005). doi: [10.1016/j.molcel.2005.08.014](https://doi.org/10.1016/j.molcel.2005.08.014); pmid: [16153868](https://pubmed.ncbi.nlm.nih.gov/16153868/)
 14. C. Vazquez, S. M. Horner, MAVS Activation of Antiviral Innate Immunity. *J. Virol.* **89**, 6974–6977 (2015). doi: [10.1128/JVI.01918-14](https://doi.org/10.1128/JVI.01918-14); pmid: [25948741](https://pubmed.ncbi.nlm.nih.gov/25948741/)
 15. M. Caudron-Herger, R. E. Jansen, E. Wassmer, S. Diederichs, RBP2GO: A comprehensive pan-species database on RNA-binding proteins, their interactions and functions. *Nucleic Acids Res.* **49**, D425–D436 (2021). doi: [10.1093/nar/gkaa1040](https://doi.org/10.1093/nar/gkaa1040); pmid: [33196814](https://pubmed.ncbi.nlm.nih.gov/33196814/)
 16. M. W. Hentze, T. Castello, T. Schwarzel, T. Preiss, A brave new world of RNA-binding proteins. *Nat. Rev. Mol. Cell Biol.* **19**, 327–341 (2018). doi: [10.1038/nrm.2017.130](https://doi.org/10.1038/nrm.2017.130); pmid: [29339797](https://pubmed.ncbi.nlm.nih.gov/29339797/)
 17. H. F. Noller, Ribosomal RNA and translation. *Annu. Rev. Biochem.* **60**, 191–227 (1991). doi: [10.1146/annurev.bi.60.070191.001203](https://doi.org/10.1146/annurev.bi.60.070191.001203); pmid: [1883196](https://pubmed.ncbi.nlm.nih.gov/1883196/)
 18. B. D. Berkovits, C. Mayr, Alternative 3' UTRs act as scaffolds to regulate membrane protein localization. *Nature* **522**, 363–367 (2015). doi: [10.1038/nature14321](https://doi.org/10.1038/nature14321); pmid: [25896326](https://pubmed.ncbi.nlm.nih.gov/25896326/)
 19. L. A. Goff, J. L. Rinn, Linking RNA biology to lncRNAs. *Genome Res.* **25**, 1456–1465 (2015). doi: [10.1101/gr.191122.115](https://doi.org/10.1101/gr.191122.115); pmid: [26430155](https://pubmed.ncbi.nlm.nih.gov/26430155/)
 20. F. Kopf, J. T. Mendell, Functional Classification and Experimental Dissection of Long Noncoding RNAs. *Cell* **172**, 393–407 (2018). doi: [10.1016/j.cell.2018.01.011](https://doi.org/10.1016/j.cell.2018.01.011); pmid: [29373828](https://pubmed.ncbi.nlm.nih.gov/29373828/)
 21. C. Mayr, What Are 3' UTRs Doing? *Cold Spring Harb. Perspect. Biol.* **11**, a034728 (2019). doi: [10.1101/cshperspect.a034728](https://doi.org/10.1101/cshperspect.a034728); pmid: [30181377](https://pubmed.ncbi.nlm.nih.gov/30181377/)
 22. I. Ulitsky, D. P. Bartel, lncRNAs: Genomics, evolution, and mechanisms. *Cell* **154**, 26–46 (2013). doi: [10.1016/j.cell.2013.06.020](https://doi.org/10.1016/j.cell.2013.06.020); pmid: [23827673](https://pubmed.ncbi.nlm.nih.gov/23827673/)
 23. M. Aznaourova et al., Noncoding RNA *Mal1* is an integral component of the TLR4-TRIF pathway. *Proc. Natl. Acad. Sci. U.S.A.* **117**, 9042–9053 (2020). doi: [10.1073/pnas.1920393117](https://doi.org/10.1073/pnas.1920393117); pmid: [32241891](https://pubmed.ncbi.nlm.nih.gov/32241891/)
 24. R. Horos et al., The Small Non-coding Vault RNA1-1 Acts as a Riboregulator of Autophagy. *Cell* **176**, 1054–1067.e12 (2019). doi: [10.1016/j.cell.2019.01.030](https://doi.org/10.1016/j.cell.2019.01.030); pmid: [30773316](https://pubmed.ncbi.nlm.nih.gov/30773316/)
 25. I. Huppertz et al., Riboregulation of Enolase 1 activity controls glycolysis and embryonic stem cell differentiation. *Mol. Cell* **82**, 2666–2680.e11 (2022). doi: [10.1016/j.molcel.2022.05.019](https://doi.org/10.1016/j.molcel.2022.05.019); pmid: [35709751](https://pubmed.ncbi.nlm.nih.gov/35709751/)
 26. Y. Luo et al., mRNA interactions with disordered regions control protein activity. *bioRxiv* 2023.02.18.529068 [Preprint] (2023); <https://doi.org/10.1101/2023.02.18.529068>
 27. X. Chen, M. M. Fansler, U. Janjó, J. Ule, C. Mayr, The FXR1 network acts as a signaling scaffold for actomyosin remodeling. *Cell* **187**, 5048–5063.e25 (2024).
 28. Y. Zhang, J. Seemann, RNA scaffolds the Golgi ribbon by forming condensates with GM130. *Nat. Cell Biol.* **26**, 1139–1153 (2024). doi: [10.1038/s41565-024-01447-2](https://doi.org/10.1038/s41565-024-01447-2); pmid: [38992139](https://pubmed.ncbi.nlm.nih.gov/38992139/)
 29. A. I. Järvelin, M. Noerenberg, I. Davis, A. Castello, The new (dis)order in RNA regulation. *Cell Commun. Signal.* **14**, 9 (2016). doi: [10.1186/s12964-016-0132-3](https://doi.org/10.1186/s12964-016-0132-3); pmid: [27048167](https://pubmed.ncbi.nlm.nih.gov/27048167/)
 30. A. Castello et al., Comprehensive Identification of RNA-Binding Domains in Human Cells. *Mol. Cell* **63**, 696–710 (2016). doi: [10.1016/j.molcel.2016.06.029](https://doi.org/10.1016/j.molcel.2016.06.029); pmid: [27453046](https://pubmed.ncbi.nlm.nih.gov/27453046/)
 31. M. Sato et al., Distinct and essential roles of transcription factors IRF-3 and IRF-7 in response to viruses for IFN- α/β gene induction. *Immunity* **13**, 539–548 (2000). doi: [10.1016/S1074-7613\(00\)00053-4](https://doi.org/10.1016/S1074-7613(00)00053-4); pmid: [11070172](https://pubmed.ncbi.nlm.nih.gov/11070172/)
 32. W. Zeng, M. Xu, S. Liu, L. Sun, Z. J. Chen, Key role of Ubc5 and lysine-63 polyubiquitination in viral activation of IRF3. *Mol. Cell* **36**, 315–325 (2009). doi: [10.1016/j.molcel.2009.09.037](https://doi.org/10.1016/j.molcel.2009.09.037); pmid: [19854139](https://pubmed.ncbi.nlm.nih.gov/19854139/)
 33. Y.-M. Loo et al., Distinct RIG-I and MDA5 signaling by RNA viruses in innate immunity. *J. Virol.* **82**, 335–345 (2008). doi: [10.1128/JVI.01080-07](https://doi.org/10.1128/JVI.01080-07); pmid: [17942531](https://pubmed.ncbi.nlm.nih.gov/17942531/)
 34. E. Genoyer et al., The Viral Polymerase Complex Mediates the Interaction of Viral Ribonucleoprotein Complexes with Recycling Endosomes during Sendai Virus Assembly. *mBio* **11**, e02028-20 (2020). doi: [10.1128/mBio.02028-20](https://doi.org/10.1128/mBio.02028-20); pmid: [32843550](https://pubmed.ncbi.nlm.nih.gov/32843550/)
 35. T. Clackson et al., Redesigning an FKBP-ligand interface to generate chemical dimerizers with novel specificity. *Proc. Natl. Acad. Sci. U.S.A.* **95**, 10437–10442 (1998). doi: [10.1073/pnas.95.18.10437](https://doi.org/10.1073/pnas.95.18.10437); pmid: [9724721](https://pubmed.ncbi.nlm.nih.gov/9724721/)
 36. T. Saito et al., Regulation of innate antiviral defenses through a shared repressor domain in RIG-I and LGP2. *Proc. Natl. Acad. Sci. U.S.A.* **104**, 582–587 (2007). doi: [10.1073/pnas.0606699104](https://doi.org/10.1073/pnas.0606699104); pmid: [17190814](https://pubmed.ncbi.nlm.nih.gov/17190814/)
 37. M. Caudron-Herger et al., R-Deep: Proteome-wide and Quantitative Identification of RNA-Dependent Proteins by Density Gradient Ultracentrifugation. *Mol. Cell* **75**, 184–199.e10 (2019). doi: [10.1016/j.molcel.2019.04.018](https://doi.org/10.1016/j.molcel.2019.04.018); pmid: [31076284](https://pubmed.ncbi.nlm.nih.gov/31076284/)
 38. S. W. Brubaker, A. E. Gauthier, E. W. Mills, N. T. Ingolia, J. C. Kagan, A bicistronic MAVS transcript highlights a class of truncated variants in antiviral immunity. *Cell* **156**, 800–811 (2014). doi: [10.1016/j.cell.2014.01.021](https://doi.org/10.1016/j.cell.2014.01.021); pmid: [24529381](https://pubmed.ncbi.nlm.nih.gov/24529381/)
 39. J. Rehwinkel et al., RIG-I detects viral genomic RNA during negative-strand RNA virus infection. *Cell* **140**, 397–408 (2010). doi: [10.1016/j.cell.2010.01.020](https://doi.org/10.1016/j.cell.2010.01.020); pmid: [20144762](https://pubmed.ncbi.nlm.nih.gov/20144762/)
 40. B. J. Zarngar et al., irCLIP platform for efficient characterization of protein-RNA interactions. *Nat. Methods* **13**, 489–492 (2016). doi: [10.1038/nmeth.3840](https://doi.org/10.1038/nmeth.3840); pmid: [27111506](https://pubmed.ncbi.nlm.nih.gov/27111506/)
 41. Y. Shi et al., An autoinhibitory mechanism modulates MAVS activity in antiviral innate immune response. *Nat. Commun.* **6**, 7811 (2015). doi: [10.1038/ncomms7811](https://doi.org/10.1038/ncomms7811); pmid: [26183716](https://pubmed.ncbi.nlm.nih.gov/26183716/)
 42. N. Qi et al., Multiple truncated isoforms of MAVS prevent its spontaneous aggregation in antiviral innate immune signalling. *Nat. Commun.* **8**, 15676 (2017). doi: [10.1038/ncomms15676](https://doi.org/10.1038/ncomms15676); pmid: [28607490](https://pubmed.ncbi.nlm.nih.gov/28607490/)
 43. G. Erdős, M. Pajkos, Z. Dosztányi, IUPred3: Prediction of protein disorder enhanced with unambiguous experimental annotation and visualization of evolutionary conservation. *Nucleic Acids Res.* **49** (W1), W297–W303 (2021). doi: [10.1093/nar/gkaa1040](https://doi.org/10.1093/nar/gkaa1040); pmid: [34048569](https://pubmed.ncbi.nlm.nih.gov/34048569/)
 44. A. Hatos et al., FuzPred: A web server for the sequence-based prediction of the context-dependent binding modes of proteins. *Nucleic Acids Res.* **51** (W1), W198–W206 (2023). doi: [10.1093/nar/gkaa214](https://doi.org/10.1093/nar/gkaa214); pmid: [36987846](https://pubmed.ncbi.nlm.nih.gov/36987846/)
 45. J. Jumper et al., Highly accurate protein structure prediction with AlphaFold. *Nature* **596**, 583–589 (2021). doi: [10.1038/s41586-021-03819-2](https://doi.org/10.1038/s41586-021-03819-2); pmid: [34265844](https://pubmed.ncbi.nlm.nih.gov/34265844/)
 46. A. Balcerak, A. Trebinska-Stryjewska, R. Konopinski, M. Wakula, E. A. Grzybowska, RNA-protein interactions: Disorder, moonlighting and junk contribute to eukaryotic complexity. *Open Biol.* **9**, 190096 (2019). doi: [10.1098/rsb.190096](https://doi.org/10.1098/rsb.190096); pmid: [32121316](https://pubmed.ncbi.nlm.nih.gov/32121316/)
 47. S. Calabretta, S. Richard, Emerging Roles of Disordered Sequences in RNA-Binding Proteins. *Trends Biochem. Sci.* **40**, 662–672 (2015). doi: [10.1016/j.tibs.2015.08.012](https://doi.org/10.1016/j.tibs.2015.08.012); pmid: [26481498](https://pubmed.ncbi.nlm.nih.gov/26481498/)
 48. P. E. Wright, H. J. Dyson, Intrinsically disordered proteins in cellular signalling and regulation. *Nat. Rev. Mol. Cell Biol.* **16**, 18–29 (2015). doi: [10.1038/nrm3920](https://doi.org/10.1038/nrm3920); pmid: [25531225](https://pubmed.ncbi.nlm.nih.gov/25531225/)
 49. R. D. Patton et al., Chemical crosslinking enhances RNA immunoprecipitation for efficient identification of binding sites of proteins that photo-crosslink poorly with RNA. *RNA* **26**, 1216–1233 (2020). doi: [10.1261/ma.074856.120](https://doi.org/10.1261/ma.074856.120); pmid: [32467309](https://pubmed.ncbi.nlm.nih.gov/32467309/)
 50. C. H. Vieira-Vieira, M. Selbach, Opportunities and Challenges in Global Quantification of RNA-Protein Interaction via UV Cross-Linking. *Front. Mol. Biosci.* **8**, 669939 (2021). doi: [10.3389/fmolb.2021.669939](https://doi.org/10.3389/fmolb.2021.669939); pmid: [34055886](https://pubmed.ncbi.nlm.nih.gov/34055886/)
 51. K. W. Brannan et al., Robust single-cell discovery of RNA targets of RNA-binding proteins and ribosomes. *Nat. Methods* **18**, 507–519 (2021). doi: [10.1038/s41592-021-01128-0](https://doi.org/10.1038/s41592-021-01128-0); pmid: [33963355](https://pubmed.ncbi.nlm.nih.gov/33963355/)
 52. M. N. Flamand, K. Ke, R. Tamming, K. D. Meyer, Single-molecule identification of the target RNAs of different RNA binding proteins simultaneously in cells. *Genes Dev.* **36**, 1002–1015 (2022). doi: [10.1101/gad.349983.122](https://doi.org/10.1101/gad.349983.122); pmid: [36302554](https://pubmed.ncbi.nlm.nih.gov/36302554/)
 53. M. Tegowski, M. N. Flamand, K. D. Meyer, scDART-seq reveals distinct m^A signatures and mRNA methylation heterogeneity in single cells. *Mol. Cell* **82**, 868–878.e10 (2022). doi: [10.1016/j.molcel.2021.12.038](https://doi.org/10.1016/j.molcel.2021.12.038); pmid: [35081365](https://pubmed.ncbi.nlm.nih.gov/35081365/)
 54. A. E. Shaw et al., Fundamental properties of the mammalian innate immune system revealed by multispecies comparison of type I interferon responses. *PLOS Biol.* **15**, e2004086 (2017). doi: [10.1371/journal.pbio.2004086](https://doi.org/10.1371/journal.pbio.2004086); pmid: [29253866](https://pubmed.ncbi.nlm.nih.gov/29253866/)
 55. R. Oughtred et al., The BioGRID database: A comprehensive biomedical resource of curated protein, genetic, and chemical interactions. *Protein Sci.* **30**, 187–200 (2021). doi: [10.1002/pro.3978](https://doi.org/10.1002/pro.3978); pmid: [33070389](https://pubmed.ncbi.nlm.nih.gov/33070389/)
 56. D. Szklarczyk et al., STRING v11: Protein-protein association networks with increased coverage, supporting functional discovery in genome-wide experimental datasets. *Nucleic Acids Res.* **47**, D607–D613 (2019). doi: [10.1093/nar/gky1131](https://doi.org/10.1093/nar/gky1131); pmid: [30476243](https://pubmed.ncbi.nlm.nih.gov/30476243/)
 57. V. K. Mootha et al., PGC-1 α -responsive genes involved in oxidative phosphorylation are coordinately downregulated in human diabetes. *Nat. Genet.* **34**, 267–273 (2003). doi: [10.1038/ng1180](https://doi.org/10.1038/ng1180); pmid: [12808457](https://pubmed.ncbi.nlm.nih.gov/12808457/)
 58. A. Subramanian et al., Gene set enrichment analysis: A knowledge-based approach for interpreting genome-wide expression profiles. *Proc. Natl. Acad. Sci. U.S.A.* **102**, 15545–15550 (2005). doi: [10.1073/pnas.0506580102](https://doi.org/10.1073/pnas.0506580102); pmid: [16199517](https://pubmed.ncbi.nlm.nih.gov/16199517/)
 59. D. Thanos, T. Maniatis, Virus induction of human IFN beta gene expression requires the assembly of an enhancerosome. *Cell* **83**, 1091–1100 (1995). doi: [10.1016/0092-8674\(95\)90136-1](https://doi.org/10.1016/0092-8674(95)90136-1); pmid: [8548797](https://pubmed.ncbi.nlm.nih.gov/8548797/)
 60. T. Saito, D. M. Owen, F. Jiang, J. Marcotrigiano, M. Gale Jr., Innate immunity induced by composition-dependent RIG-I recognition of hepatitis C virus RNA. *Nature* **453**, 523–527 (2008). doi: [10.1038/nature07106](https://doi.org/10.1038/nature07106); pmid: [18548002](https://pubmed.ncbi.nlm.nih.gov/18548002/)
 61. C. He et al., High-Resolution Mapping of RNA-Binding Regions in the Nuclear Proteome of Embryonic Stem Cells. *Mol. Cell* **64**, 416–430 (2016). doi: [10.1016/j.molcel.2016.09.034](https://doi.org/10.1016/j.molcel.2016.09.034); pmid: [27768875](https://pubmed.ncbi.nlm.nih.gov/27768875/)
 62. A. A. Pai et al., Widespread Shortening of 3' Untranslated Regions and Increased Exon Inclusion Are Evolutionarily Conserved Features of Innate Immune Responses to Infection. *PLOS Genet.* **12**, e1006338 (2016). doi: [10.1371/journal.pgen.1006338](https://doi.org/10.1371/journal.pgen.1006338); pmid: [27690314](https://pubmed.ncbi.nlm.nih.gov/27690314/)
 63. Y. Ge et al., Downregulation of CPSF6 leads to global mRNA 3'UTR shortening and enhanced antiviral immune responses. *PLOS Pathog.* **20**, e1020621 (2024). doi: [10.1371/journal.ppat.1020621](https://doi.org/10.1371/journal.ppat.1020621); pmid: [38416782](https://pubmed.ncbi.nlm.nih.gov/38416782/)
 64. V. Bergant et al., mRNA 3'UTR lengthening by alternative polyadenylation attenuates inflammatory responses and correlates with virulence of Influenza A virus. *Nat. Commun.* **14**, 4906 (2023). doi: [10.1038/s41467-023-40469-6](https://doi.org/10.1038/s41467-023-40469-6); pmid: [37582777](https://pubmed.ncbi.nlm.nih.gov/37582777/)
 65. R. J. Carlson, M. D. Leiken, A. Guna, N. Hacohen, P. C. Blainey, A genome-wide optical pooled screen reveals regulators of cellular antiviral responses. *Proc. Natl. Acad. Sci. U.S.A.* **120**, e2210623120 (2023). doi: [10.1073/pnas.2210623120](https://doi.org/10.1073/pnas.2210623120); pmid: [37043539](https://pubmed.ncbi.nlm.nih.gov/37043539/)
 66. R. Zhang et al., The Endoplasmic Reticulum ATP13A1 is Essential for MAVS-Mediated Antiviral Innate Immunity. *Adv. Sci.* **9**, e2203831 (2022). doi: [10.1002/advs.202203831](https://doi.org/10.1002/advs.202203831); pmid: [36216581](https://pubmed.ncbi.nlm.nih.gov/36216581/)
 67. N. S. Gokhale, J. R. Smith, R. D. Van Gelder, R. Savan, RNA regulatory mechanisms that control antiviral innate immunity. *Immunol. Rev.* **304**, 77–96 (2021). doi: [10.1111/imr.13019](https://doi.org/10.1111/imr.13019); pmid: [34405416](https://pubmed.ncbi.nlm.nih.gov/34405416/)

68. J. C. Kagan, V. G. Magupalli, H. Wu, SMOCs: Supramolecular organizing centres that control innate immunity. *Nat. Rev. Immunol.* **14**, 821–826 (2014). doi: [10.1038/nri3757](https://doi.org/10.1038/nri3757); pmid: [25359439](https://pubmed.ncbi.nlm.nih.gov/25359439/)
69. B. L. Fredericksen, M. Gale Jr., West Nile virus evades activation of interferon regulatory factor 3 through RIG-I-dependent and -independent pathways without antagonizing host defense signaling. *J. Virol.* **80**, 2913–2923 (2006). doi: [10.1128/JVI.80.6.2913-2923.2006](https://doi.org/10.1128/JVI.80.6.2913-2923.2006); pmid: [16501100](https://pubmed.ncbi.nlm.nih.gov/16501100/)
70. F. W. Soveg *et al.*, Endomembrane targeting of human OAS1 p46 augments antiviral activity. *eLife* **10**, e71047 (2021). doi: [10.7554/eLife.71047](https://doi.org/10.7554/eLife.71047); pmid: [34342578](https://pubmed.ncbi.nlm.nih.gov/34342578/)
71. H. M. Froggatt, A. T. Harding, R. R. Chaparian, N. S. Heaton, ETV7 limits antiviral gene expression and control of influenza viruses. *Sci. Signal.* **14**, eabe1194 (2021). doi: [10.1126/scisignal.abe1194](https://doi.org/10.1126/scisignal.abe1194); pmid: [34257104](https://pubmed.ncbi.nlm.nih.gov/34257104/)
72. F. Heigwer, G. Kerr, M. Boutros, E-CRISP: Fast CRISPR target site identification. *Nat. Methods* **11**, 122–123 (2014). doi: [10.1038/nmeth.2812](https://doi.org/10.1038/nmeth.2812); pmid: [24481216](https://pubmed.ncbi.nlm.nih.gov/24481216/)
73. O. Shalem *et al.*, Genome-scale CRISPR-Cas9 knockout screening in human cells. *Science* **343**, 84–87 (2014). doi: [10.1126/science.1247005](https://doi.org/10.1126/science.1247005); pmid: [24336571](https://pubmed.ncbi.nlm.nih.gov/24336571/)
74. J. Schindelin *et al.*, Fiji: An open-source platform for biological-image analysis. *Nat. Methods* **9**, 676–682 (2012). doi: [10.1038/nmeth.2019](https://doi.org/10.1038/nmeth.2019); pmid: [22743772](https://pubmed.ncbi.nlm.nih.gov/22743772/)
75. A. Horvath, M. Miskei, V. Ambrus, M. Vendruscolo, M. Fuhrer, Sequence-based prediction of protein binding mode landscapes. *PLoS Comput. Biol.* **16**, e1007864 (2020). doi: [10.1371/journal.pcbi.1007864](https://doi.org/10.1371/journal.pcbi.1007864); pmid: [32453748](https://pubmed.ncbi.nlm.nih.gov/32453748/)
76. Y. Chen *et al.*, SOAPnuke: A MapReduce acceleration-supported software for integrated quality control and preprocessing of high-throughput sequencing data. *Gigascience* **7**, 1–6 (2018). doi: [10.1093/gigascience/gjx120](https://doi.org/10.1093/gigascience/gjx120); pmid: [29220494](https://pubmed.ncbi.nlm.nih.gov/29220494/)
77. FastQC (2015). <https://qubeshub.org/resources/fastqc>.
78. P. Ewels, M. Magnusson, S. Lundin, M. Käller, MultiQC: Summarize analysis results for multiple tools and samples in a single report. *Bioinformatics* **32**, 3047–3048 (2016). doi: [10.1093/bioinformatics/btw354](https://doi.org/10.1093/bioinformatics/btw354); pmid: [27312411](https://pubmed.ncbi.nlm.nih.gov/27312411/)
79. P. Danecek *et al.*, Twelve years of SAMtools and BCFtools. *Gigascience* **10**, giab008 (2021). doi: [10.1093/gigascience/giab008](https://doi.org/10.1093/gigascience/giab008); pmid: [33590861](https://pubmed.ncbi.nlm.nih.gov/33590861/)
80. H. P. Martin Morgan, Rsamtools, Bioconductor (2017); <https://doi.org/10.18129/B9.bioc.RSAMTOOLS>.
81. A. R. Quinlan, I. M. Hall, BEDTools: A flexible suite of utilities for comparing genomic features. *Bioinformatics* **26**, 841–842 (2010). doi: [10.1093/bioinformatics/btq033](https://doi.org/10.1093/bioinformatics/btq033); pmid: [20110278](https://pubmed.ncbi.nlm.nih.gov/20110278/)
82. R. K. Dale, B. S. Pedersen, A. R. Quinlan, Pybedtools: A flexible Python library for manipulating genomic datasets and annotations. *Bioinformatics* **27**, 3423–3424 (2011). doi: [10.1093/bioinformatics/btr539](https://doi.org/10.1093/bioinformatics/btr539); pmid: [21949271](https://pubmed.ncbi.nlm.nih.gov/21949271/)
83. F. Mölder *et al.*, Sustainable data analysis with Snakemake. *F1000Res.* **10**, 33 (2021). doi: [10.12688/f1000research.290322.2](https://doi.org/10.12688/f1000research.290322.2); pmid: [34035898](https://pubmed.ncbi.nlm.nih.gov/34035898/)
84. A. Dobin *et al.*, STAR: Ultrafast universal RNA-seq aligner. *Bioinformatics* **29**, 15–21 (2013). doi: [10.1093/bioinformatics/bts635](https://doi.org/10.1093/bioinformatics/bts635); pmid: [23104886](https://pubmed.ncbi.nlm.nih.gov/23104886/)
85. M. G. Kluesner *et al.*, MultiEditR: The first tool for the detection and quantification of RNA editing from Sanger sequencing demonstrates comparable fidelity to RNA-seq. *Mol. Ther. Nucleic Acids* **25**, 515–523 (2021). doi: [10.1016/j.omtn.2021.07.008](https://doi.org/10.1016/j.omtn.2021.07.008); pmid: [34589274](https://pubmed.ncbi.nlm.nih.gov/34589274/)
86. J. Rappaport, M. Mann, Y. Ishihama, Protocol for micro-purification, enrichment, pre-fractionation and storage of peptides for proteomics using StageTips. *Nat. Protoc.* **2**, 1896–1906 (2007). doi: [10.1038/nprot.2007.261](https://doi.org/10.1038/nprot.2007.261); pmid: [17703201](https://pubmed.ncbi.nlm.nih.gov/17703201/)
87. A. T. Kong, F. V. Leprevost, D. M. Avtonomov, D. Mellacheruvu, A. I. Nesvizhskii, MSFragger: Ultrafast and comprehensive peptide identification in mass spectrometry-based proteomics. *Nat. Methods* **14**, 513–520 (2017). doi: [10.1038/nmeth.4256](https://doi.org/10.1038/nmeth.4256); pmid: [28394336](https://pubmed.ncbi.nlm.nih.gov/28394336/)
88. V. Demichev, C. B. Messner, S. I. Verbitskiy, K. S. Lilley, M. Ralser, DIA-NN: Neural networks and interference correction enable deep proteome coverage in high throughput. *Nat. Methods* **17**, 41–44 (2020). doi: [10.1038/s41592-019-0638-x](https://doi.org/10.1038/s41592-019-0638-x); pmid: [31768060](https://pubmed.ncbi.nlm.nih.gov/31768060/)
89. S. Tyanova *et al.*, The Perseus computational platform for comprehensive analysis of (proteo)omics data. *Nat. Methods* **13**, 731–740 (2016). doi: [10.1038/nmeth.3901](https://doi.org/10.1038/nmeth.3901); pmid: [27348712](https://pubmed.ncbi.nlm.nih.gov/27348712/)
90. D. Mellacheruvu *et al.*, The CRAPome: A contaminant repository for affinity purification-mass spectrometry data. *Nat. Methods* **10**, 730–736 (2013). doi: [10.1038/nmeth.2557](https://doi.org/10.1038/nmeth.2557); pmid: [23921808](https://pubmed.ncbi.nlm.nih.gov/23921808/)
91. N. T. Doncheva, J. H. Morris, J. Gorodkin, L. J. Jensen, Cytoscape StringApp: Network Analysis and Visualization of Proteomics Data. *J. Proteome Res.* **18**, 623–632 (2019). doi: [10.1021/acs.jproteome.8b00702](https://doi.org/10.1021/acs.jproteome.8b00702); pmid: [30450911](https://pubmed.ncbi.nlm.nih.gov/30450911/)
92. P. Shannon *et al.*, Cytoscape: A software environment for integrated models of biomolecular interaction networks. *Genome Res.* **13**, 2498–2504 (2003). doi: [10.1101/gr.123930.3](https://doi.org/10.1101/gr.123930.3); pmid: [14597658](https://pubmed.ncbi.nlm.nih.gov/14597658/)
93. D. Merico, R. Isserlin, O. Stueker, A. Emili, G. D. Bader, Enrichment map: A network-based method for gene set enrichment visualization and interpretation. *PLOS ONE* **5**, e13984 (2010). doi: [10.1371/journal.pone.0013984](https://doi.org/10.1371/journal.pone.0013984); pmid: [21085593](https://pubmed.ncbi.nlm.nih.gov/21085593/)

ACKNOWLEDGMENTS

We thank N. Heaton, J. Hyde, K. Meyer, D. Shechner, Y. Sancak, D. Stetson, C. Vazquez, and K. Labagnara for reagents and/or helpful discussion. We also thank D. Dauphars, P. Fink, and

all members of the Savan lab for manuscript review and editing.

Funding: National Institutes of Health grant K99AI175483 (N.S.G.); National Institutes of Health grant R01AI153246 (A.O.); National Institutes of Health grant R01AI155512 (S.M.H.); National Institutes of Health grant R01AI125416 (S.M.H.); National Institutes of Health grant R01GM129090 (S.E.O.); National Institutes of Health grant R01AI145296 (M.G.); National Institutes of Health grant R21AI158788 (M.G.); National Institutes of Health grant R01AI175724 (R.S.); National Institutes of Health grant R21AI176442 (R.S.); National Institutes of Health grant R21AI141823 (R.S.); National Institutes of Health S1G grant S10OD021502 (S.E.O.); National Institutes of Health grant F32AI176736 (E.G.); National Institutes of Health grant T32AI07140 (J.E.); Helen Hay Whitney Postdoctoral Fellowship F1266 (N.S.G.); American Cancer Society Postdoctoral Fellowship PF-21-117-01ORMC (M.G.T.). **Author contributions:** Conceptualization: N.S.G., R.S.; Investigation: N.S.G., R.K.S., K.S., M.G.T., D.M.M., J.R.S., E.G., J.E.; Methodology: N.S.G., K.S., M.G.T., S.D., M.P., L.H.C., D.M.M., S.E.O.; Formal analysis: N.S.G., K.S., M.G.T., D.M.M.; Software: N.S.G., K.S., M.G.T., D.M.M.; Visualization: N.S.G., K.S., M.G.T.; Resources: N.S.G., A.O., S.M.H., S.E.O., M.G., R.S.; Writing – original draft: N.S.G.; Writing – review and editing: N.S.G., R.K.S., K.S., M.G.T., D.M.M., J.R.S., E.G., J.E., L.H.C., S.D., A.O., S.M.H., S.E.O., M.G., R.S.; Funding acquisition: N.S.G., M.G.T., E.G., J.E., A.O., S.M.H., S.E.O., M.G., R.S. **Competing interests:** M.G. is a founder and shareholder in Kinetix Inc. and HDT Bio. The other authors declare that they have no competing interests. **Data and materials availability:** All data needed to evaluate the conclusions in the paper are present in the paper or the supplementary materials. Raw APOBEC1-mediated profiling data have been submitted and are available through the Gene Expression Omnibus (GSE24400). Raw mass spectrometry data have been deposited to and are available through the MassIVE repository (MSV000092912). Any plasmids or cell lines generated in this study are available from the corresponding authors upon completion of a Materials Transfer Agreement. **License information:** Copyright © 2024 the authors, some rights reserved; exclusive licensee American Association for the Advancement of Science. No claim to original US government works. <https://www.science.org/about/science-licenses-journal-article-reuse>

SUPPLEMENTARY MATERIALS

science.org/doi/10.1126/science.adl0429

Figs. S1 to S10

MDAR Reproducibility Checklist

Data S1 to S3

Submitted 25 September 2023; resubmitted 12 August 2024

Accepted 7 November 2024

10.1126/science.adl0429